Scientific Excellence • Resource Protection & Conservation • Benefits for Canadians
Excellence scientifique • Protection et conservation des ressources • Bénéfices aux Canadiens

Sea Ice Observations during LIMEX, March - April 1989

W.D. Winsor, G.B. Crocker, R.K. McKenna, and C.L. Tang

Published by:

Physical and Chemical Sciences
Scotia-Fundy Region
Bedford Institute of Oceanography

Department of Fisheries and Oceans
P.O. Box 1006, Dartmouth, N.S.
Canada B2Y 4A2

June 1990

Canadian Data Report of Hydrography and Ocean Sciences No. 81

Fisheries and Oceans | Pêches et Océans

Canada

Canadian Data Report Of Hydrography and Ocean Sciences

Data reports provide a medium for the documentation and dissemination of data in a form directly useable by the scientific and engineering communities. Generally, the reports contain raw and / or analyzed data but will not contain interpretations of the data. Such compilations commonly will have been prepared in support of work related to the programs and interests of the Ocean Science and Surveys (OSS) sector of the Department of Fisheries and Oceans.

Data reports are not intended for general distribution and the contents must not be referred to in other publications without prior written authorization from the issuing establishment. The correct citation appears above the abstract of each report. Data reports are abstracted in *Aquatic Sciences and Fisheries Abstracts* and indexed in the Department's annual index to scientific and technical publications.

Data reports are produced regionally but are numbered nationally. Requests for individual reports will be filled by the issuing establishment listed on the front cover and title page. Out of stock reports will be supplied for a fee by commercial agents.

Regional and headquarters establishments of Ocean Science and Surveys ceased publication of their various report series as of December 1981. A complete listing of these publications is published in the *Canadian Journal of Fisheries and Aquatic Sciences*, Volume 39: Index to Publications 1982. The current series, which begins with report number 1, was initiated in January 1982.

Rapport statistique canadien sur l'hydrographie et les sciences océaniques

Les rapports statistiques servent de véhicule pour la compilation et la diffusion des données sous une forme directement utilisable par les scientifiques et les techniciens. En général, les rapports contiennent des données brutes ou analysées, mais ne fournissent pas d'interprétation des données. Ces compilations sont préparées le plus souvent à l'appui de travaux liés aux programmes et intérêts du service des Sciences et levés océaniques (SLO) du ministère des Pêches et des Océans.

Les rapports statistiques ne sont pas destinés à une vaste distribution et leur contenu ne doit pas être mentionné dans une publication sans une autorisation écrite préalable de l'établissement auteur. Le titre exact paraît au-dessus du résumé de chaque rapport. Les rapports statistiques sont résumés dans la revue *Résumés des sciences halieutiques et aquatiques*, et ils sont classés dans l'index annuel des publications scientifiques et techniques du Ministère.

Les rapports statistiques sont produits à l'échelon régional, mais numérotés à l'échelon national. Les demandes de rapports seront satisfaites par l'établissement auteur dont le nom figure sur la couverture et la page du titre. Les rapports épuisés sont fournis contre rétribution par des agents commerciaux.

Les établissements des Sciences et levés océaniques dans les régions et à l'administration centrale ont cessé de publier leurs diverses séries de rapports en décembre 1981. Une liste complète de ces publications figure dans le volume 39, Index des publications 1982, du *Journal canadien des sciences halieutiques et aquatiques*. La série actuelle a commencé avec la publication du rapport numéro 1 en janvier 1982.

Canadian Data Report of
Hydrography and Ocean Sciences No. 81

June 1990

Sea Ice Observations during LIMEX, March - April 1989

by

W. D. Winsor,[1] G. B. Crocker,[1] R. F. McKenna [2] and C. L. Tang

Physical and Chemical Sciences Branch
Scotia-Funday Region
Department of Fisheries and Oceans
Bedford Institute of Oceanography
Dartmouth, NS, CANADA, B2Y 4A2

1. Centre for Cold Oceans Resources Engineering
   Memorial University of Newfoundland
   St. John's, NF, CANADA, A1B 3X5

2. Faculty of Engineering and Applied Science
   Memorial University of Newfoundland
   St. John's, NF, CANADA, A1B 3X5

Acknowledgements

We would like to thank the participants of the LIMEX '89 research cruises: to Captain R. Keeping, the officers and crew of the *M/V Terra Nordica* the RADARSAT Office, the Jet Propulsion Laboratory, the Canadian Coast Guard, and to David Lapp and Associates for their cooperation from project planning, the field program, and data reporting. The research was supported by the Panel of Energy Research and Development.

In addition, funding for the project was provided from the UP Fund, DSS Contract FP953-8-0218/01-OSC for wave induced ice motion, by J.I. Clark from an NSERC CRD Grant, by I.J. Jordaan from the NSERC/Mobil Industrial Research Chair in Ocean Engineering at Memorial University. Compression testing equipment was provided by the Institute for Research in Construction of National Research Council of Canada (NRCC) through the courtesy of R.M.W. Frederking who, along with N.K. Sinha, gave helpful suggestions regarding testing procedures. The use of the portable cold room belonging to the Institute for Marine Dynamics of NRCC is appreciated.

Cat. No.FS 97-16/81 E, ISSN 0711-6721

Correct citation for this publication:
Winsor, W.D., G.B. Crocker, R.F. McKenna, and C.L. Tang. 1990. Sea Ice Observations during LIMEX, March - April 1989. Canadian Data Report of Hydrography and Ocean Sciences No. 81: iv + 43 pp.

Contents

Abstract

Winsor, W.D., G.B. Crocker, R.F. McKenna, and C.L. Tang. 1990. Sea Ice Observations during LIMEX, March - April 1989. Canadian Data Report of Hydrography and Ocean Sciences No. 81: iv + 43 pp.

Data of sea ice properties collected on *M/V Terra Nordica* during LIMEX'89 (Labrador Ice Margin Experiment) are documented. The data include ice thickness, ice drift, ice temperature and salinity, ice strength, and floe size distribution. Statistics and geographic distribution of these parameters are displayed.

Résumé

Winsor, W.D., G.B. Crocker, R.F. McKenna, and C.L. Tang. 1990. Sea Ice Observations during LIMEX, March - April 1989. Canadian Data Report of Hydrography and Ocean Sciences No. 81: iv + 43 pp.

On commente ici les données sur les propriétés de la glace marine recueillies par le *Terra Nordica*, lors de l'Étude de la zone marginale des glaces du Labrador (LIMEX 89). Elles portent notamment sur l'épaisseur, sur la dérive, sur la température, sur la salinité et sur la résistance le la glace, ainsi que sur la distribution de la banquise selon la taille. On présente des ventilations géographiques et statistiques de ces paramètres.

1 Introduction:

An engineered structure deployed in ice infested waters is vulnerable to static and dynamic forces caused by sea ice. Engineers are concerned with the interactions of the ice and the structure. In the design of the structure, at least two conditions must be considered: (1) response to extreme events that may test whether the structure remains steadfast or succumbs to damage; and (2) behaviour under normal loading conditions. To understand ice-structure interaction, information on ice mass, ice movement, meteorological forcing, ice features and mechanics are required as basis for laboratory or numerical studies. This report presents ice properties data collected on the northern Grand Banks and Newfoundland shelf during the Labrador Ice Margin Experiment in March and April 1989 (LIMEX '89), (Carsey *et al* 1989).

Sea ice strength depends on such ice properties as temperature, salinity, crystal size and orientation, and bubble distribution. Ice forces can be characterized in terms of failure mode such as bending and crushing, and ice and structure geometry. While various yield criteria and failure theories have been proposed for specific applications, and model testing has been used extensively in designing structures, the shortcomings in modelling ice properties and the lack of standard testing procedures hamper both the interpretation of model test results and comparsion between different investigations. The basis for extrapolating small scale laboratory test data to field conditions requires further development and verification. Accurate information on the physical characteristics of ice is likely to lead to cost-effective designs and help form a basis for the establishment of appropriate certification guidelines.

The LIMEX 89 field program provided an extensive example of ice conditions encountered of the Labrador marginal ice zone. Because of the seasonal variability over this region the data collected must be viewed as one type of offshore ice which can develop. The ice cover was distinct from the ice cover encountered during the LIMEX '87 pilot project. During 1989, the ice cover extended to 48 N, 47.5 W on Julian Day (JD) 82 (March 23) and to 48 N, 47 W by JD 93 (April 3). The ice cover at the eastern edge was disperse and composed of small floes, not suitable for ice operations. By contrast in 1987, the ice margin displayed a well defined ice edge with thick stable ice floes right to the boundary.

LIMEX '89 was made up of three research cruises: the *M/V Terra Nordica* from JD 65 to 79 (March 6 to 20), *CCGS Sir John Franklin* from JD 71 to 76 (March 12 to 17), and the *M/V Terra Nordica* Phase II from JD 83 to 92 (March 23 to April 2). The document draws on the ice conditions data collect by the three phases of the LIMEX '89 program. The report concentrates on the activities of the third component, *M/V Terra Nordica* Phase II where the authors conducted the ice properties portion of the cruise. Figure 1 shows a map of the offshore region considered. The boundaries of operational areas for the three cruises are plotted and labeled. The ice edge mapped by Atmospheric Environmental Service, Ice Centre overflights, JD 70 and JD 86, shows the extent the ice coverage through the experimental period. The

ice cover concentration varied over the region and changed through the time period of the cruises. A shore lead and light ice conditions along coast persisted through most of the study period.

Section 2 provides the ice thickness measurements from all three phases. The drift data from the ice beacons deployed during the third cruise is reported in Section 3. The ice cover air temperature records were collected in conjunction with the ice motion records. These and the collected ice temperature measurements are reported in Section 4. Ice salinities were measure on all three segments of the experiment and are reported in Section 5.

The ice strength work from phase II on the *M/V Terra Nordica* is documented in Section 6. The ice cover description for the final component of the experiment is covered in Section 7. The characterization of the ice cover by the airborne remote sensing with the synethic aperture radar is beyond the scope of the contract.

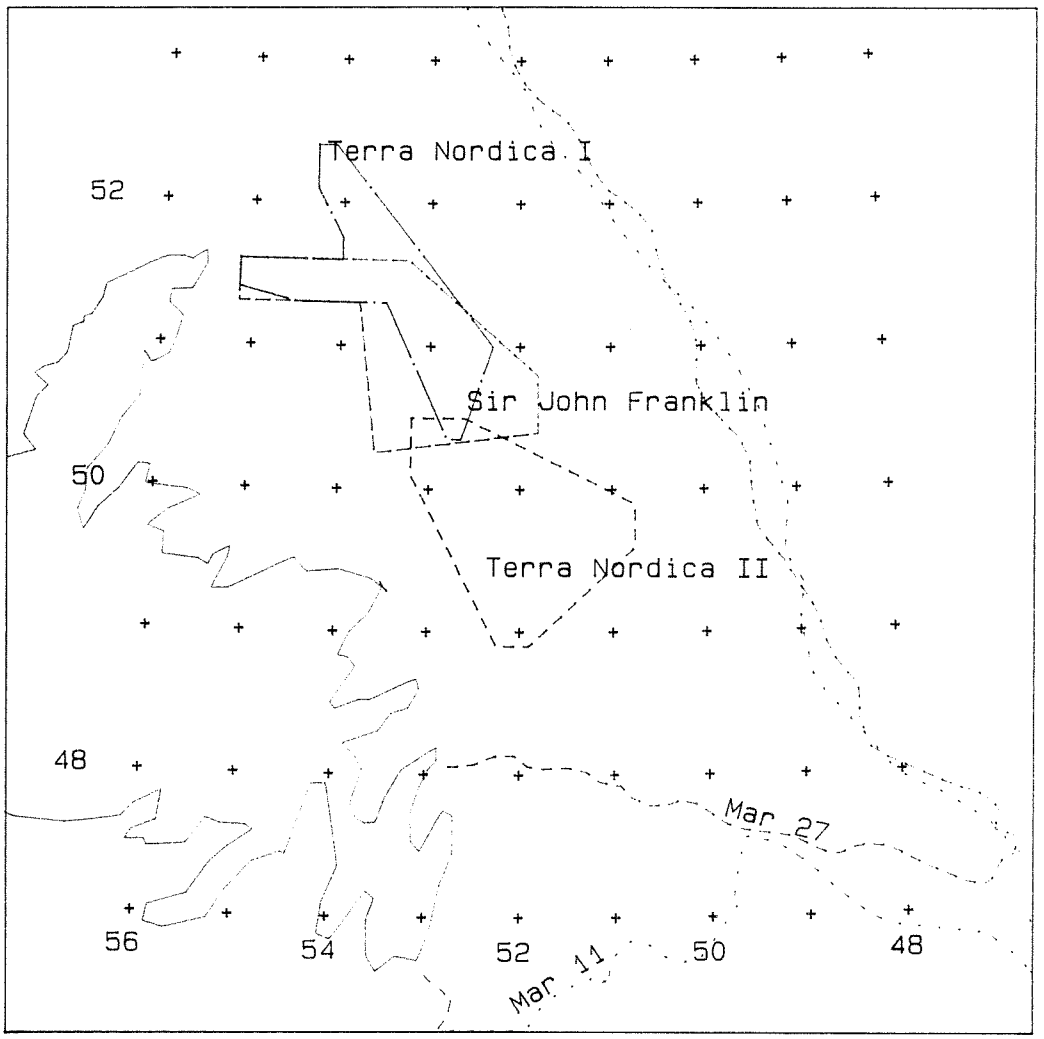

Figure 1: Map of operational area for the LIMEX '89 cruises. The ice cover extended east to longnitude *49 W*. The floe sizes were small adjacent to the eastern edge.

2 Ice Thickness:

Two type of ice thickness measurements were conducted during LIMEX'89. Auger drilled ice thicknesses measurements were carried out from each of the three phases of the experiment. Just over 100 samples were collected during each phase of the fieldwork.

There was several ice thicknesses measured at many of the ice stations. Measurement replication is valuable because thickness variation within individual floes and for adjacent floes is an important characteristic of sea ice cover. Drilling several holes at each station provides an estimate of the thickness distribution for the of sea ice cover. The second method of ice thicknesses demonstrated for LIMEX'89 was the Canpolar Inc's. ice thickness remote sensing program. A helicopter overflight collected thickness samples along a number of flight lines. These ice thickness profiles are plotted in the LIMEX'89 data report. The remote thickness data are not easily integrated with the auger ice thickness program conducted from the ships. As indicated by Rossiter (1989) augered ice thickness values tend to be biased. The field team can not sample thin floes because it is unsafe to drill auger hole from the floes. In the final phase of the experiment, many of the thickness values were collected from floes being checked to for ice motion package deployment, hence contributing to the bias of measuring the average floe within the cover rather than random sampling of floes. The southern region, south of *50.5 N* had about 5 percent concentration of ridge debris material. This material was much thicker than the surrounding level ice floes. None of the material was drilled to make an ice thickness measurement.

There were 99 distinct ice sampling stations and a total of 347 ice thickness samples collected. The samples were collected over a 26 day period from Julian day 67 to 92. Figure 2 show the spatial sampling coverage on a map of the offshore area covered by the field experiment. The ice thickness data was sorted into half degree blocks by latitude. The mean thickness of the grouped data is shown on Figure 3 and the maximum ice thickness encountered given in Figure 4. The number of thickness measurements included in each is plotted below the sub-group value. There are three cases where only a single sample comprises the group.

The data summary for mean thickness and standard deviation for the spatially sorted drilled ice thickness data is shown in Table 1. Histograms for the ice thickness values are plotted for each half degree block containing in excess of 25 samples. The resulting plots are given in Figures 5 to 9. A constant thickness and relative frequency ranges are assigned to facilitate comparison between blocks.

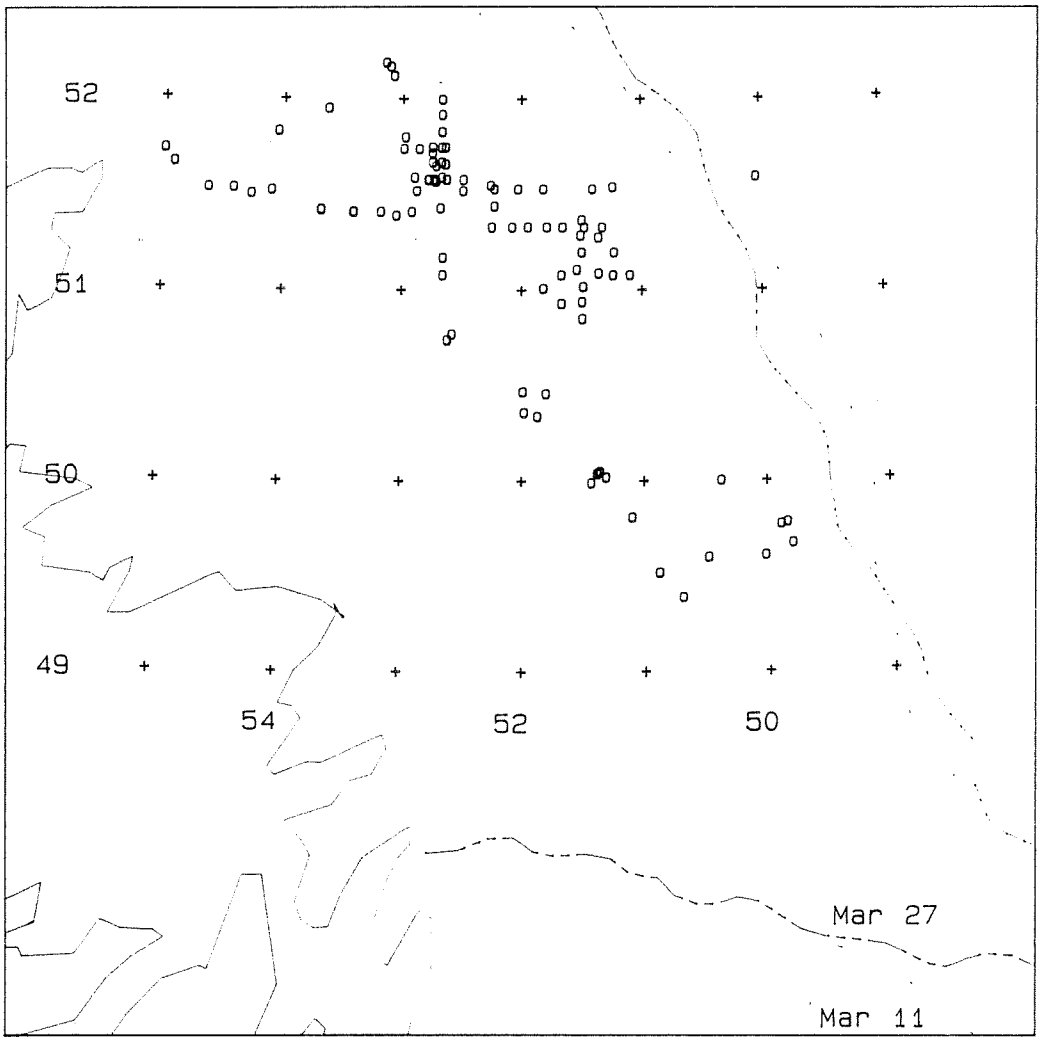

Figure 2: An area map showing positions where ice thickness auger holes were drilled. The map grid opposite corners are *49 N 49 W* and *53 N 55 W* (Lambert conformal projection).

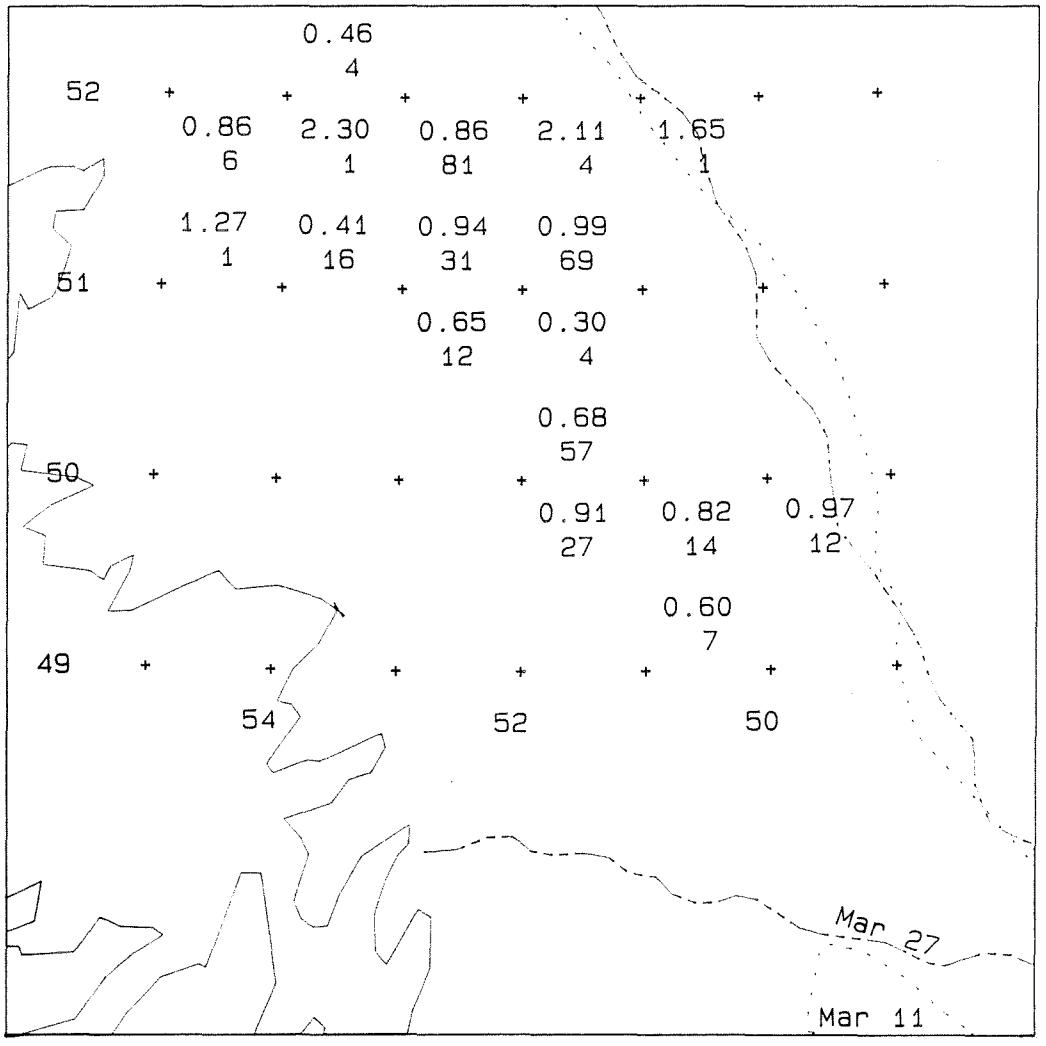

Figure 3: The distribution of mean ice thickness measured, sorted into half degree blocks by latitude. The results are presented as over and under pairs, the upper value is the mean thickness and the lower the sample count.

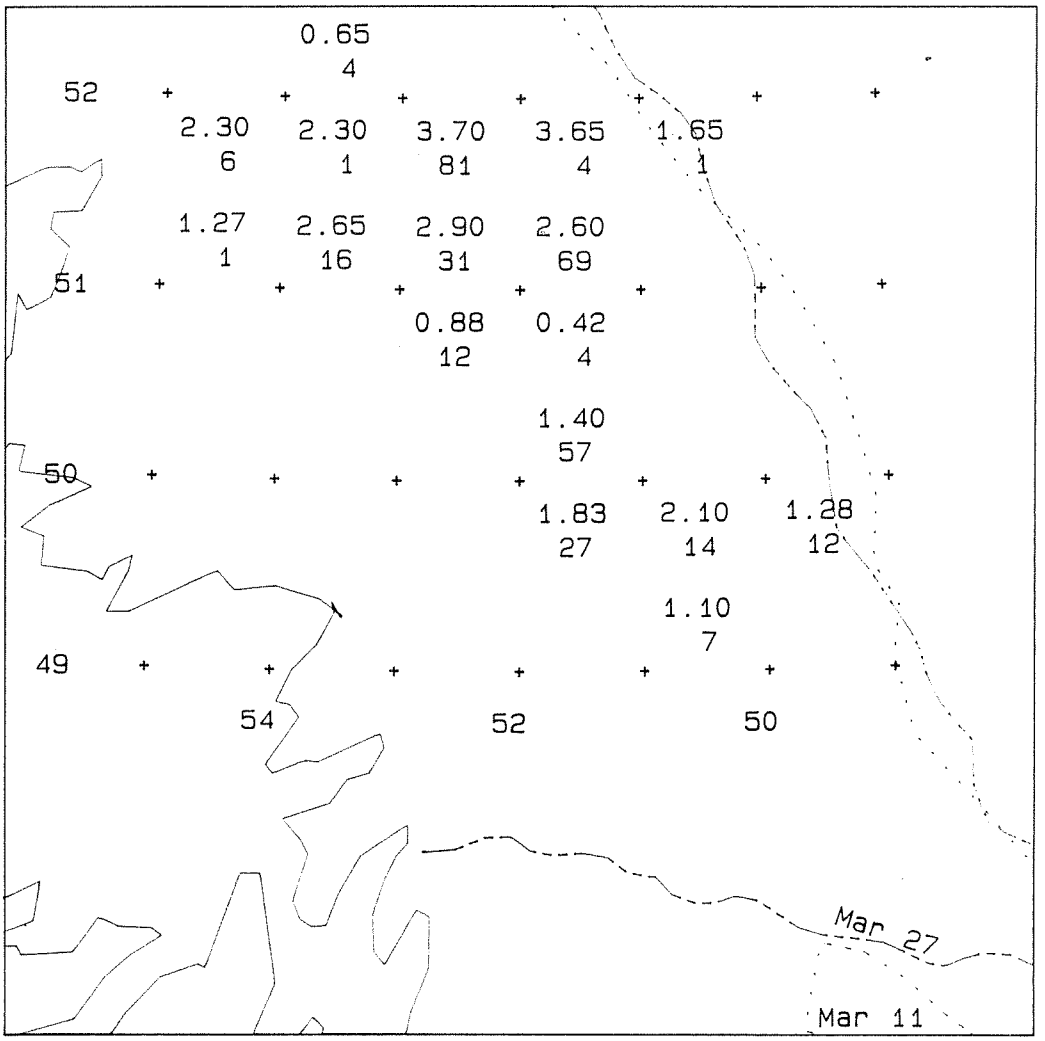

Figure 4: Similar map to to the figure above showing the extreme values ice thickness measured. The second number is the samples per half degree block.

Table 1: Summary of the grouped thickness data

latitude	longitude	average thickness m	standard deviation m	number
49.25 N	51.50 W	0.60	0.21	7
49.75 N	50.50 W	0.97	0.14	12
49.75 N	51.50 W	0.82	0.51	14
49.75 N	52.50 W	0.91	0.40	27
50.25 N	52.50 W	0.68	0.22	57
50.75 N	52.50 W	0.30	0.14	4
50.75 N	53.50 W	0.65	0.22	12
51.25 N	52.50 W	0.99	0.52	69
51.25 N	53.50 W	0.94	0.64	31
51.25 N	54.50 W	0.41	0.60	16
51.25 N	55.50 W	1.27	0.00	1
51.75 N	51.50 W	1.65	0.00	1
51.75 N	52.50 W	2.11	1.07	4
51.75 N	53.50 W	0.86	0.65	81
51.75 N	54.50 W	2.30	0.00	1
51.75 N	55.50 W	0.86	0.66	6
52.25 N	54.50 W	0.46	0.15	4

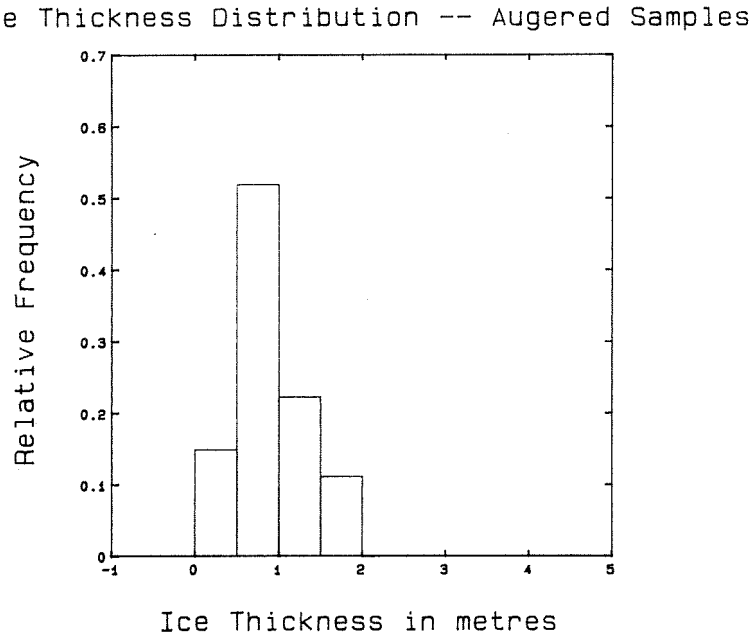

Figure 5: Histogram of ice thickness values per half degree block: block *49.5 N 52 W* to *50 N 53 W*, mean thickness 0.91 m and sample count N=27.

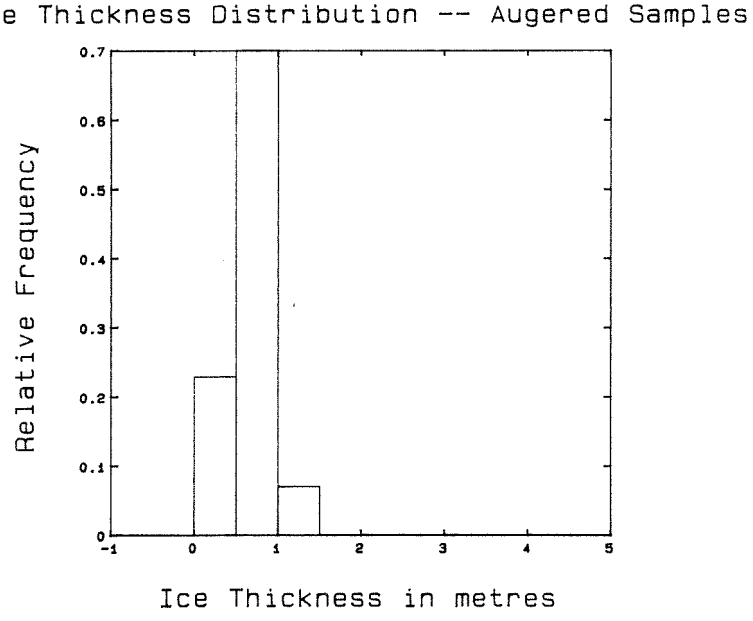

Figure 6: The histogram of ice thickness values for block *50 N 52 W* to *50.5 N 53 W*, mean thickness 0.68 m and N=57.

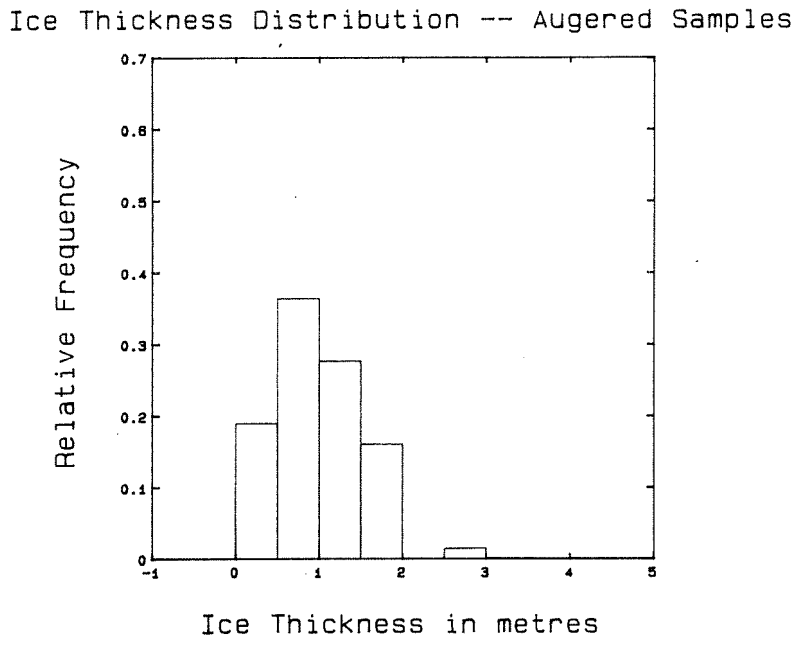

Figure 7: The histogram of ice thickness values for block *51 N 51 W* to *51.5 N 52 W*, mean thickness 0.99 m and N=69.

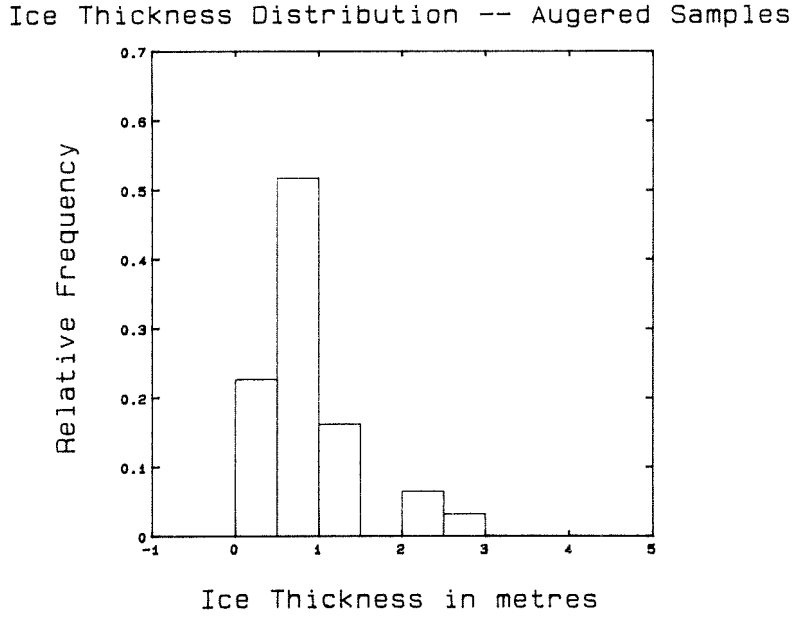

Figure 8: The histogram of ice thickness values for block *51 N 52 W* to *51.5 N 53 W*, mean thickness 0.94 m and N=31.

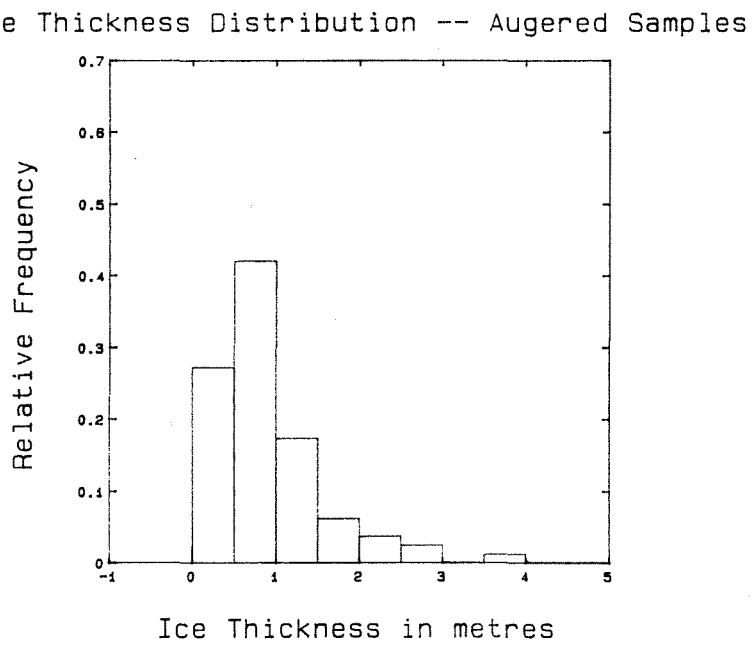

Figure 9: The histogram of ice thickness values for block 51.5 N 63 W to 52 N 54 W, mean thickness 0.86 m and N=81.

3 Sea Ice Drift:

Ice cover drift was provided with the combination of the three Bedford Institue of Oceanography ice beacons and the ARGOS transmitters on three of the six ice motion packages through phase II of the *M/V Terra Nordica* research cruise. There were fifteen deployments of ARGOS transmitters over the experimental period. Over 235 positional records were recorded. Drift rates were computed from time and position data and spurious data points (high drift rates) were manually removed leaving 235 values. The set of ARGOS buoy positions collected are plotted on an operations area map in Figure 10. The full displacement of each buoy deployment is plotted in Figure 11. The time of deployment and time of recovery for a portion of the drift tracks is plotted in Julian Days. Table 2 gives the data summary for the fifteen ice drift deployments. The set of ice drift rates and drift bearings has been sorted into half degree blocks by latitude. The mean drift rate and its standard deviation is calculated for each block. The spatial variation of mean drift rates is plotted on the map in Figure 12 and the data summary in Table 2. Histograms showing drift rate and drift bearing distributions are graphed in Figures 13 to 16.

The deployments were made sequentially over the experiment period, hence spatial variation of the drift data is also spread over the time of the data collection. Therefore the spatial variation of the mean drift bearing reflects the wind direction and the ice condition for the sampling interval. The more interesting statistic derived from the ice drift bearing data is the wide spread in the data. The direction of the short term drift is weather dominated while the longer term drift is from northwest to southeast as expected.

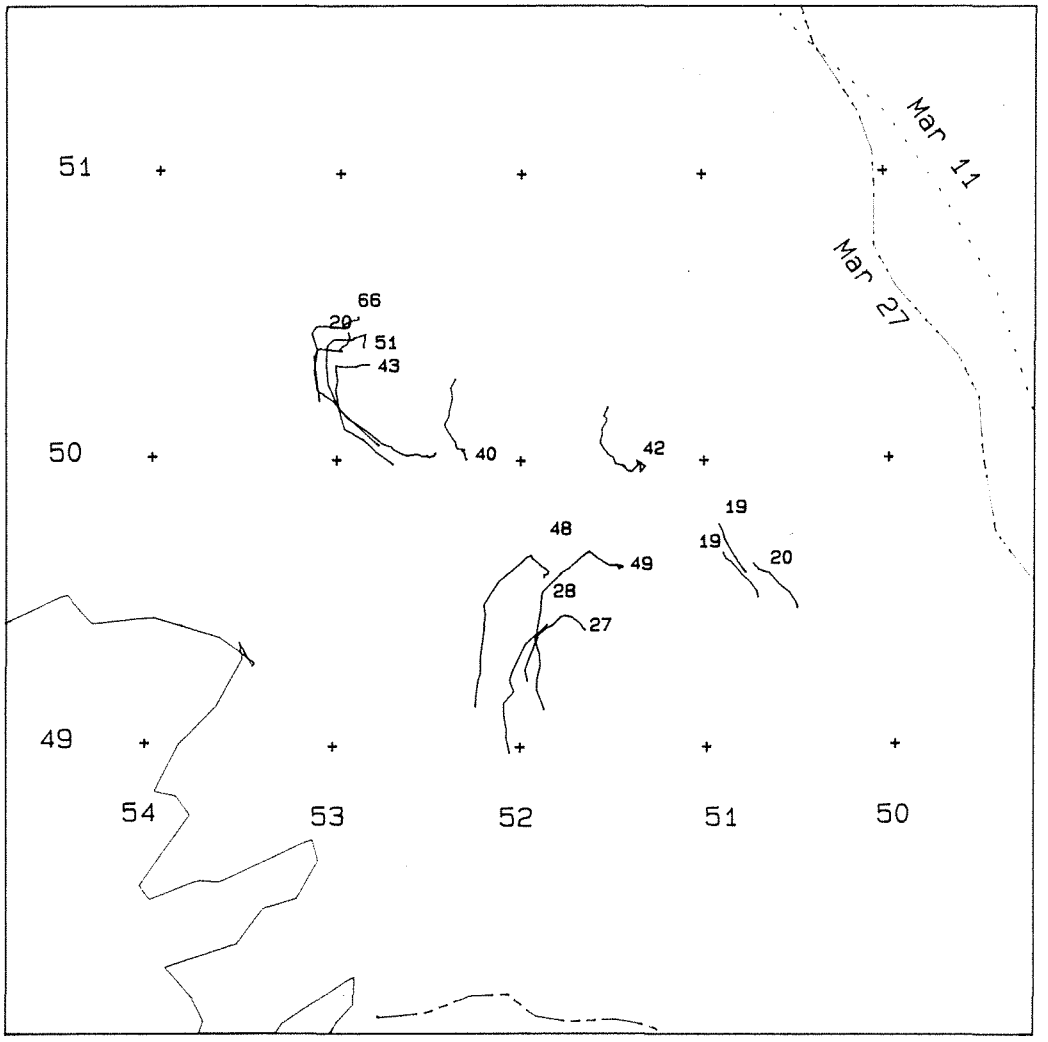

Figure 10: Map of operation area with the ARGOS buoy positions collected during the experiment plotted. The map grid opposite corners are *49 N 50 W* and *51 N 54 W* (Lambert conformal projection).

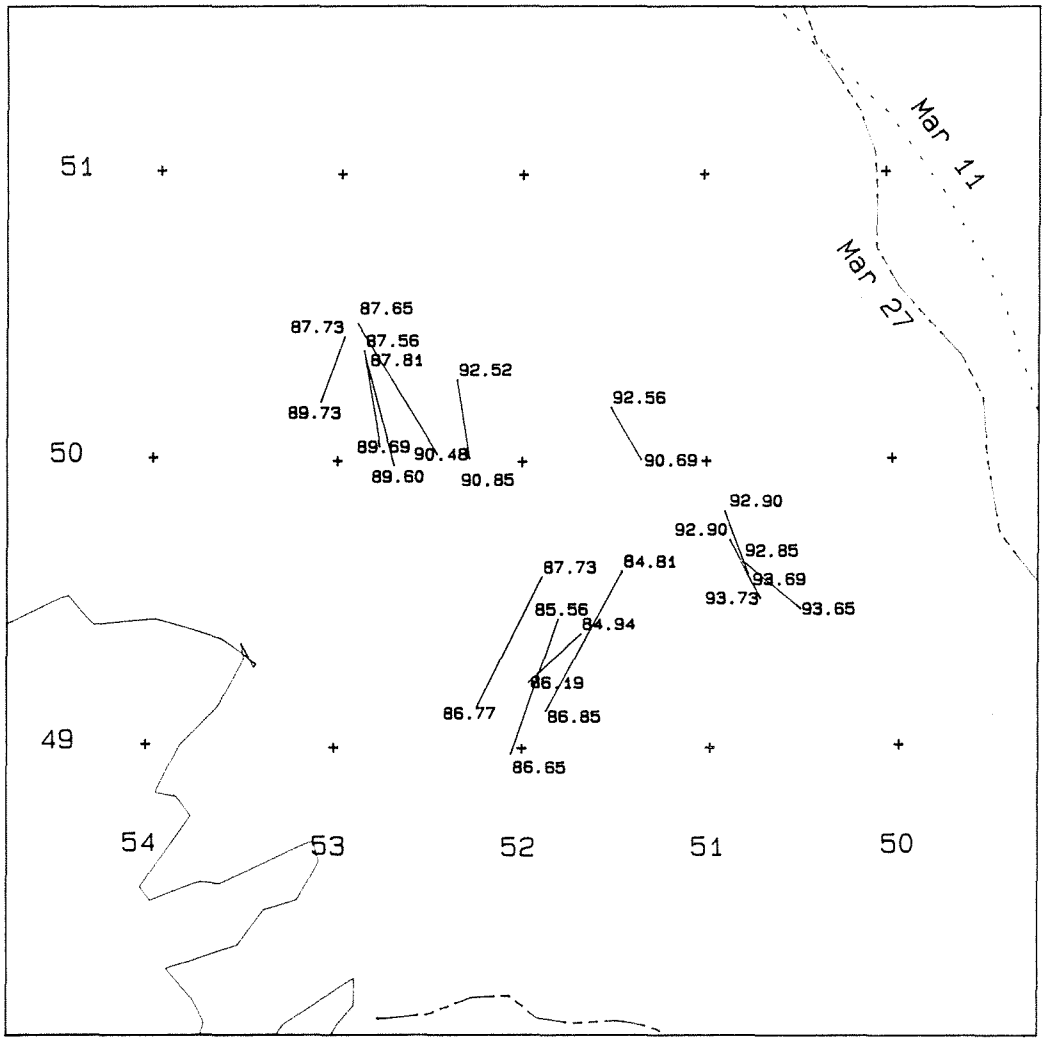

Figure 11: The map shows the total drift for each ice beacon deployment. The values accompanying the drift sticks are the deployment and recovery time of the associated end point for a beacon's drift.

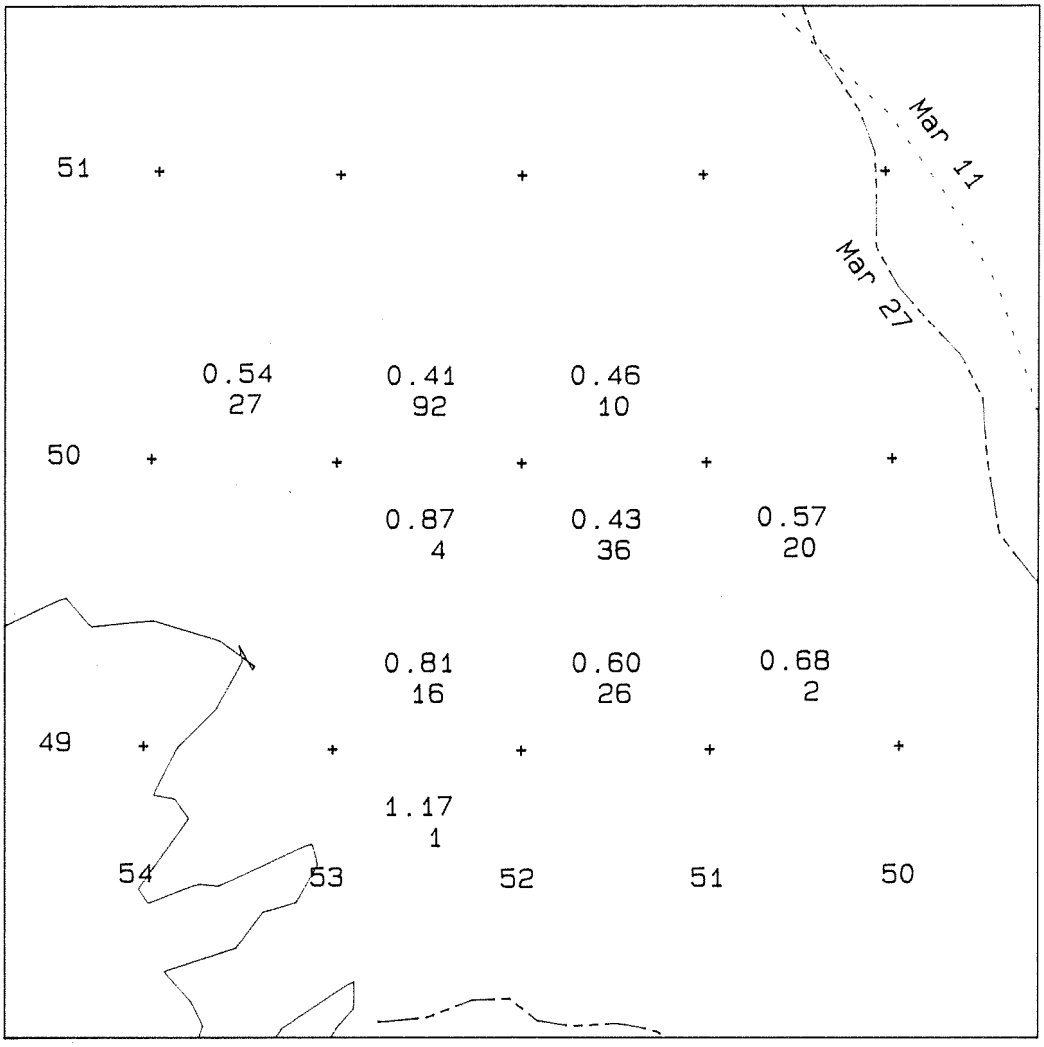

Figure 12: Area map with the magnitude of ice drifts sorted by half degree blocks, the numbers are over and under pair with the drift rate is in m/s and the number of drift rates measure per block.

Table 2: Summary of the grouped ice drift data

latitude	longitude	average drift spd m/s	standard deviation m/s	number
48.75 N	52.50 W	1.17	0.00	1
49.25 N	50.50 W	0.68	0.20	2
49.25 N	51.50 W	0.60	0.39	26
49.25 N	52.50 W	0.81	0.36	16
49.75 N	50.50 W	0.57	0.19	20
49.75 N	51.50 W	0.43	0.35	36
49.75 N	52.50 W	0.87	0.37	4
50.25 N	51.50 W	0.46	0.15	10
50.25 N	52.50 W	0.41	0.30	92
50.25 N	53.50 W	0.54	0.34	27

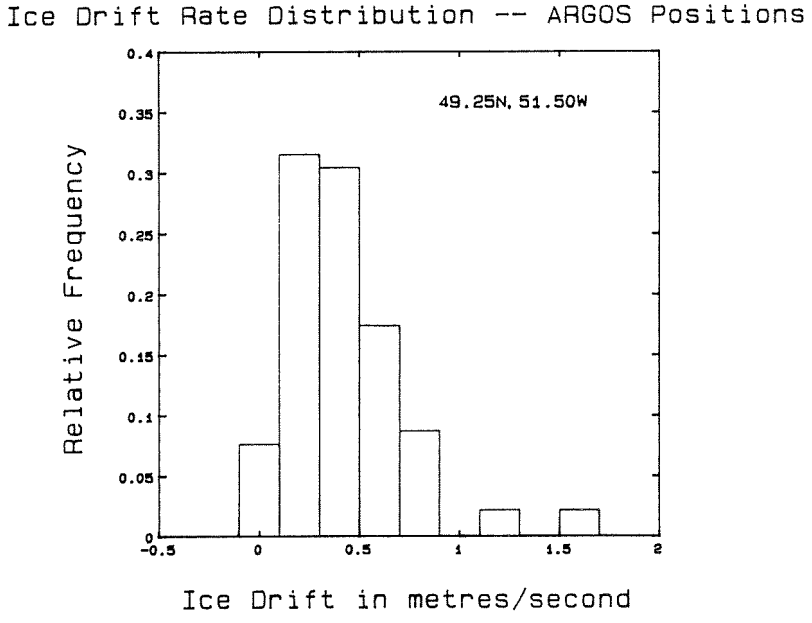

Figure 13: An histogram of the ice drift rates observed for ice beacons, sorted into half degree blocks within the cover. Block *49 N 51 W* to *49.5 N 52 W*, mean drift 0.60 m/s, N=26.

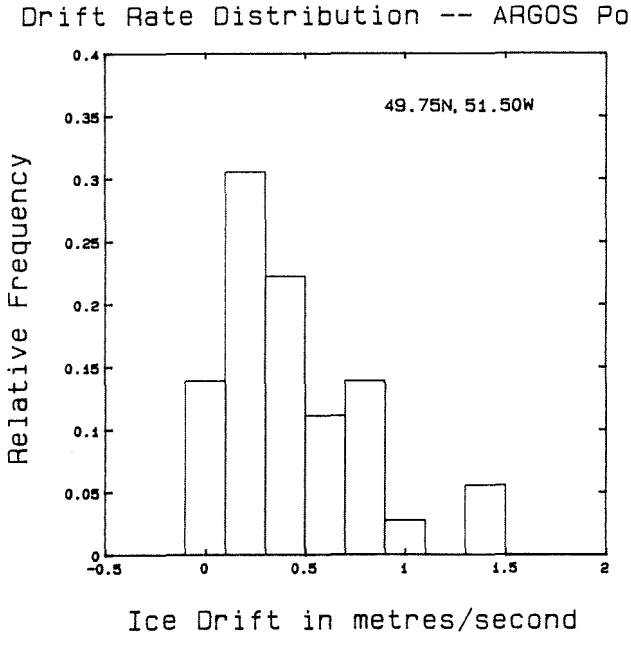

Figure 14: An histogram of the ice drift rates observed for ice beacons. Block *49.5 N 51 W* to *50 N 52 W*, mean drift 0.43 m/s, N=36.

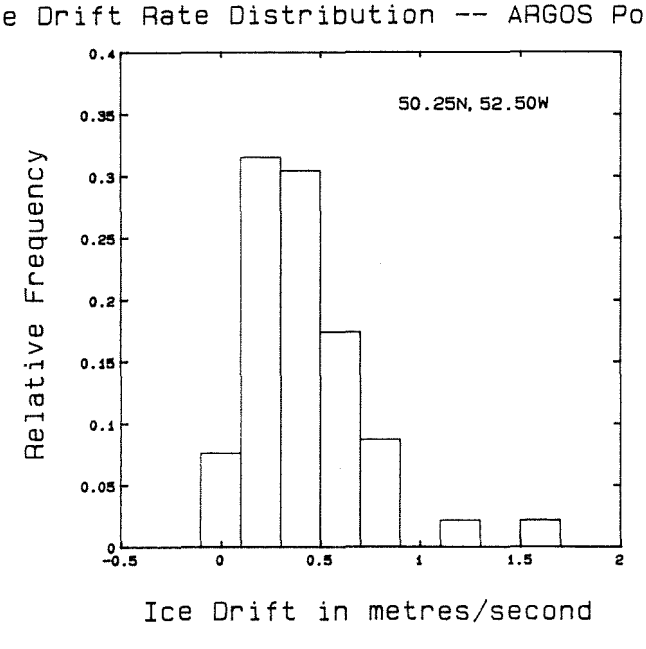

Figure 15: An histogram of the ice drift rates observed for the ice beacons. Block *50 N 52 W* to *50.5 N 53 W*, mean drift 0.41 m/s, N=92.

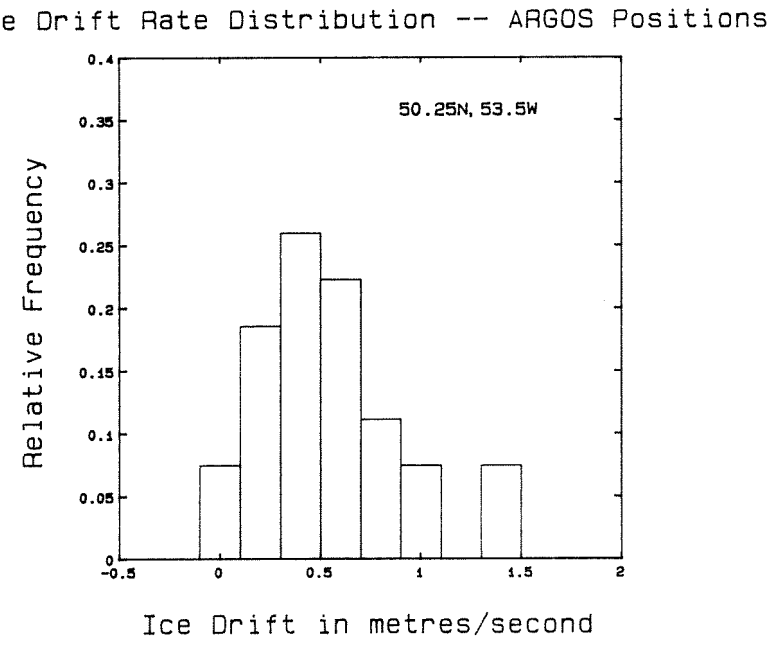

Figure 16: An histogram of the ice drift rates observed for the ice beacons. Block *49.5 N 53 W* to *50 N 54 W*, mean drift 0.54 m/s, N=27.

4 Air and Ice Temperature:

The ice motion packages were equipped a temperature probe mounted on the exterior of container. The probe was a thermistor mounted inside a radiation shield. Hence there were extensive air temperature records collected at the ice surface for the period from JD 82 (March 23) to JD 93 (April 3). The air temperature was recorded in the header block of the ice motion data. The full temperature records have been sub-sampled on a 30 minute interval for display in this report. The single longest run of temperature data is plotted when a group of ice motion packages were deployed together. The majority of the ice motion data was collected for 30 minute intervals. The first and final temperature value for each interval are used.

The air temperature is weather dependent and a time varying value, hence the temperatures are presented as time series. The air temperature are grouped into five blocks which correspond to the deployments of the ice motion packages. Ice motion experiment 4 and 5 were sequential and the temperature is grouped in a single run. The spatial data of where the air temperature is collected is provided in the figure captions. The temperature from the ice motion package which recorded the longest time series is utilized. The time base is converted to fractional Julian Day. These temperature records display the varied weather pattern encountered through the experimental period. The temperature time series are presented in Figures 17 to 21.

Sea ice and air temperature were reported for the ice characterization studies from the *CCGS Sir John Franklin* (Nazarenko & Lapp, 1989). The reported data is plotted in Figure 22. The time base for the temperature are coarse, the authors only report the operations periods on the ice, not the time the temperature reading was recorded. The mean air and ice temperatures were estimated and plotted against the mid-period time for the on ice work. Ice surface temperature correlate with air temperature, leading or lagging dependent on the prior air temperature history. Ice surface temperature is leading (colder) than air temperature during some phase of a warming trend and lagging the air temperature during a cooling trend.

Only a small number (four) of ice temperature profiles were measured during the LIMEX '89 cruises. Temperature profiles were measured for four ice cores. The surface ice temperatures are plotted as single points on Figures 18 proceeding the air temperature record and again in Figure 20 two points proceeding the air temperature record. The ice temperature profiles (Figure 23 show the surface and intermediate temperatures following the air temperature while the temperature at the ice/ocean interface remaining near the freezing point of sea water (-1.8 C).

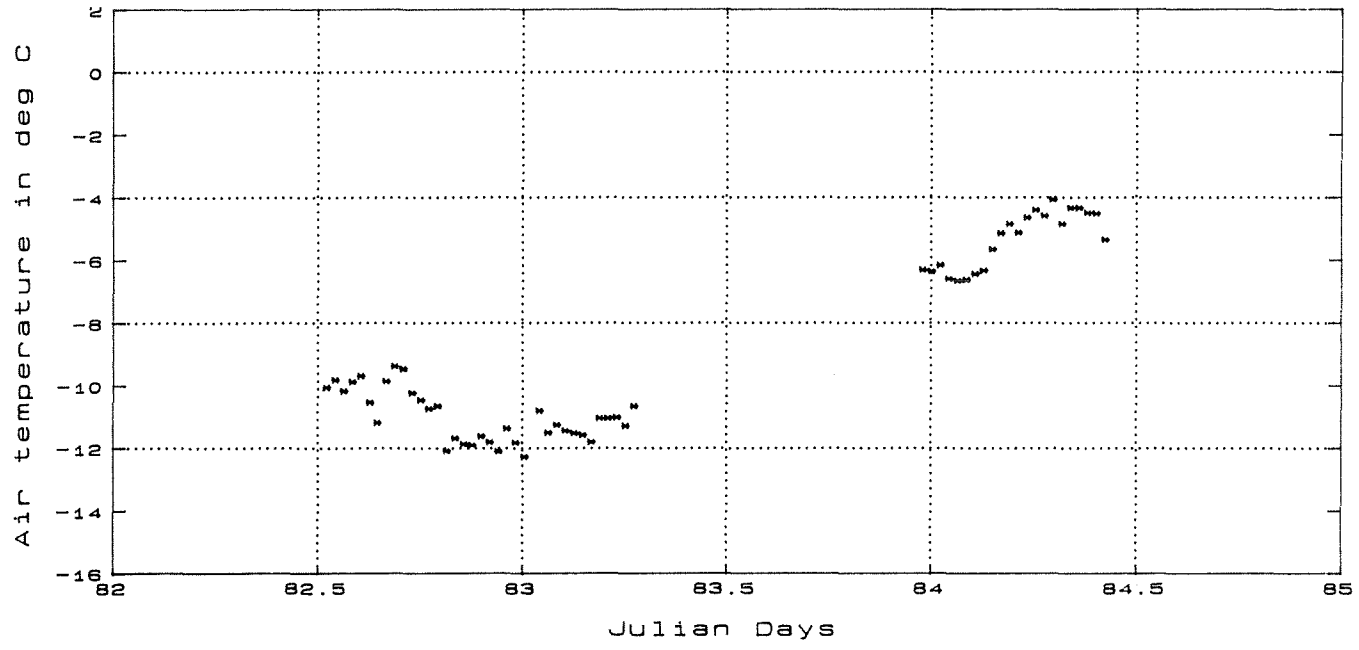

Figure 17: Temperature time series from JD 82.5 (March 23) to JD 84.5 (March 25), operation area *49 N 51 W* to *50 N 52.5 W*.

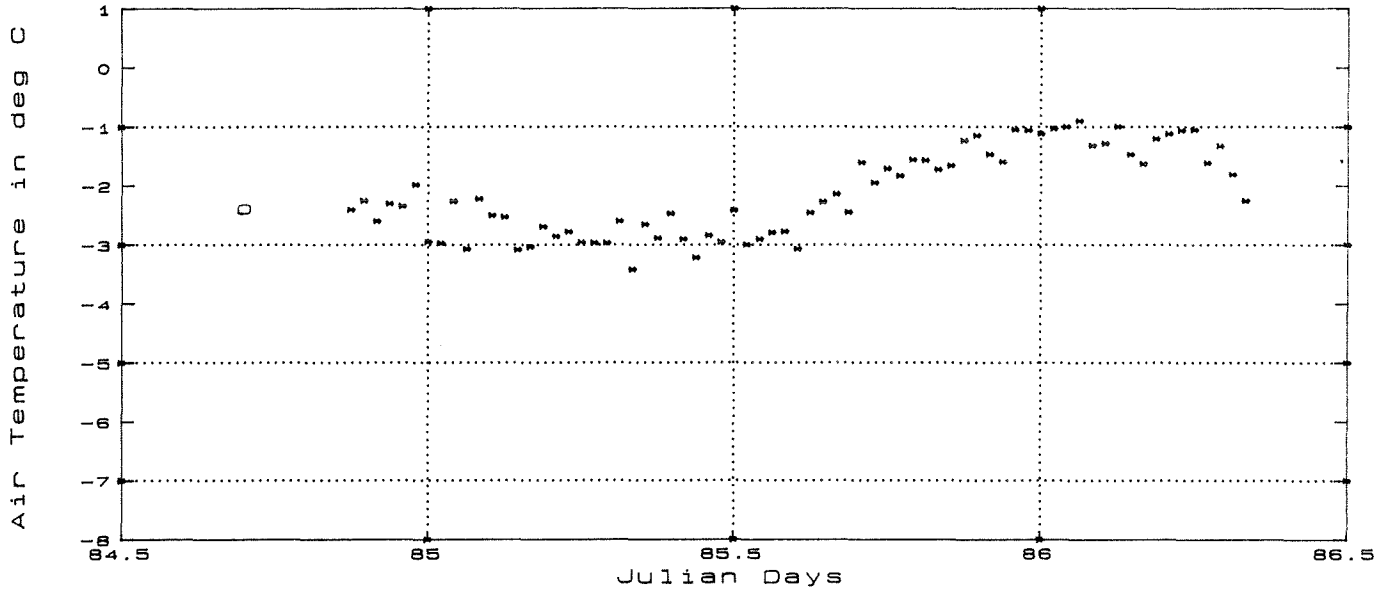

Figure 18: Temperature time series from JD 84.5 (March 25) to JD 86.5 (March 27), operation area *49 N 51 W* to *50 N 52.5 W*. The single point to the left of the time series is ice surface temperature measurement.

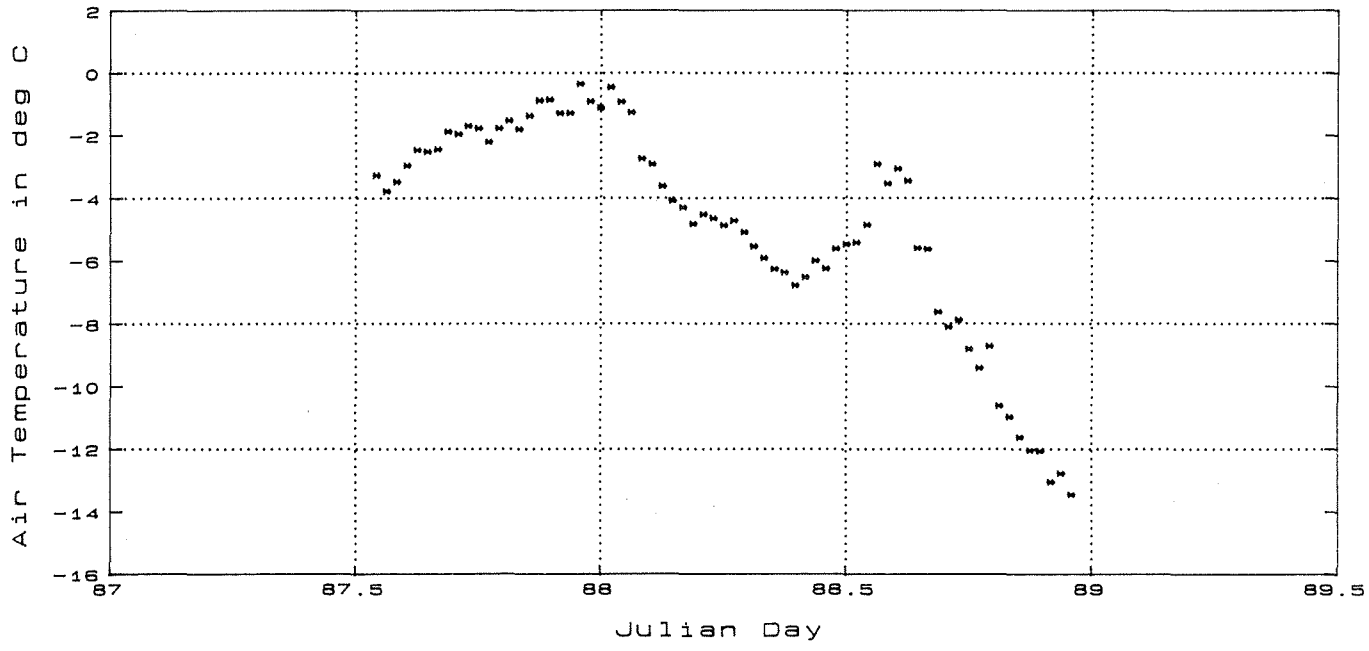

Figure 19: Temperature time series from JD 87.5 (March 28) to JD 89 (March 30), operation area *50 N 52 W* to *50.5 N 53 W*,

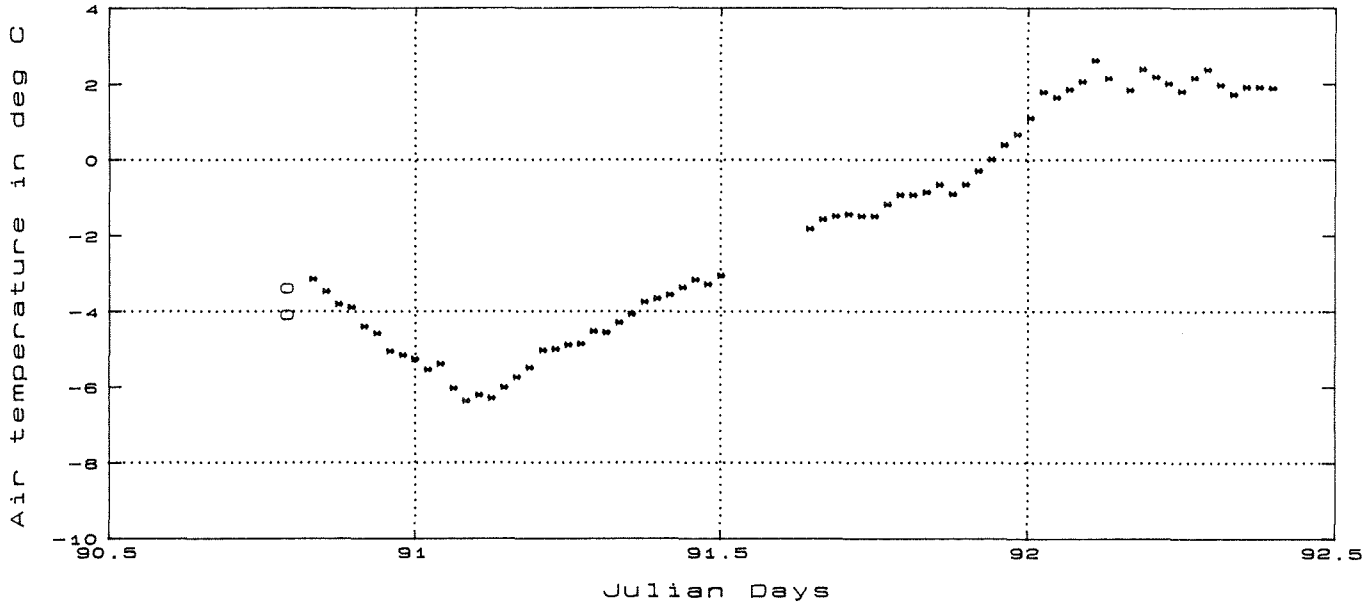

Figure 20: Temperature time series from JD 90.5 (March 31) to JD 92.5 (April 2), operation area *50 N 51 W* to *50.5 N 52 W*. The two points to the left of the time series in are ice surface temperature measurement.

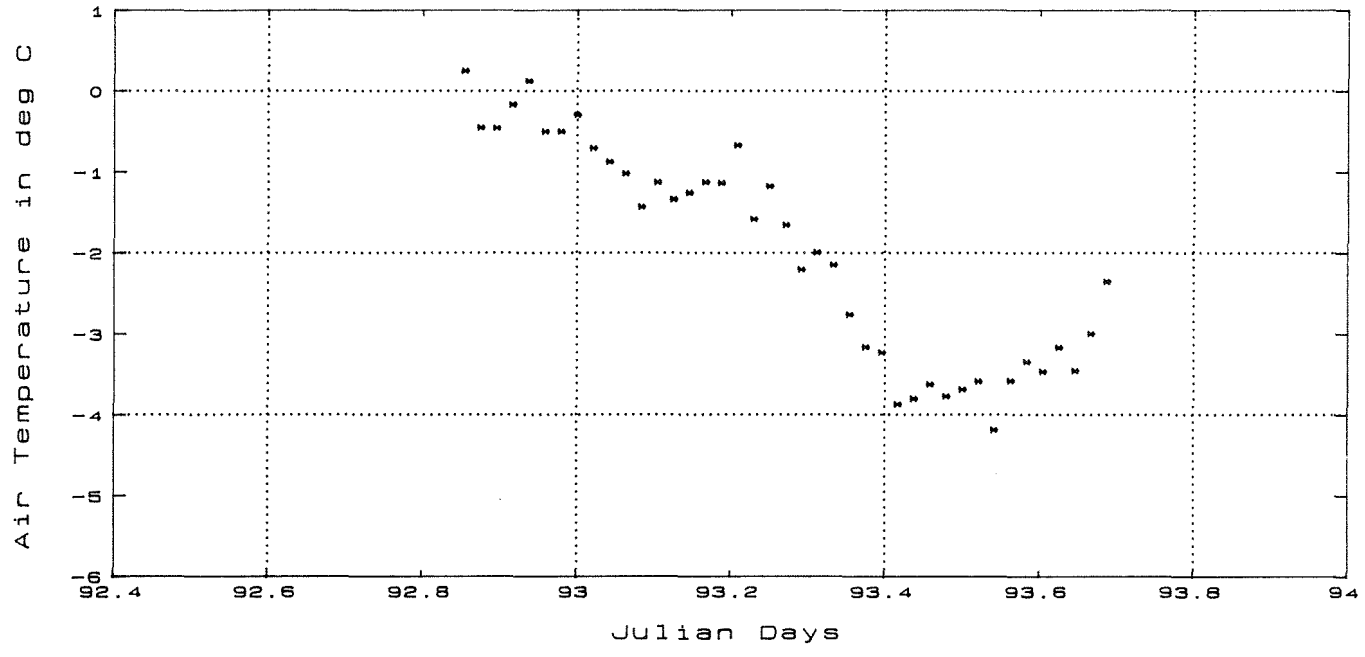

Figure 21: Temperature time series from JD 92.8 (April 2) to JD 89 (April 3), operation area *49.5 N 50 W* to *50 N 51 W*.

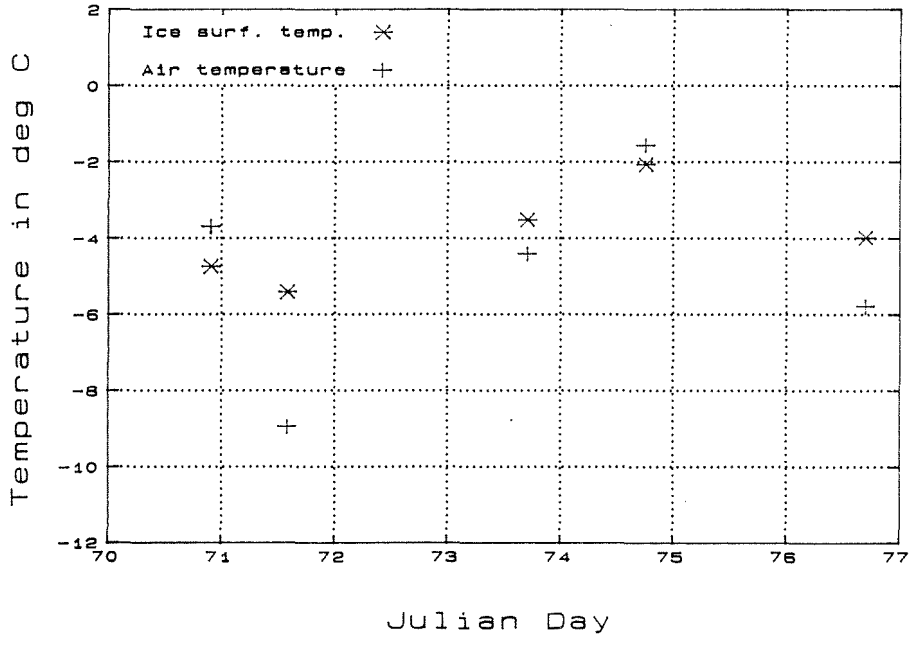

Figure 22: Ice surface and air temperatures measurements collection by the ice research team from the *CCGS Sir John Franklin*.

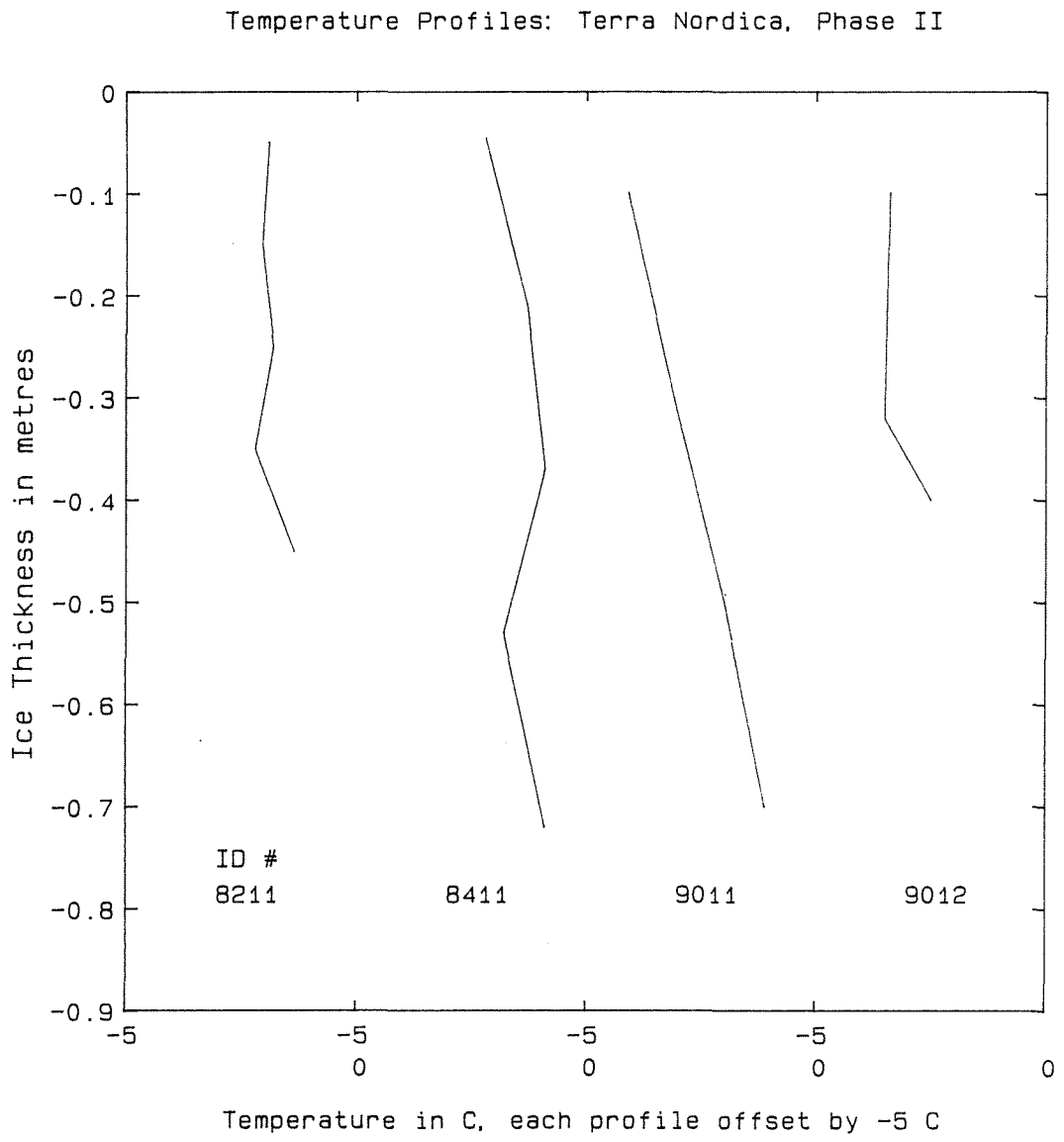

Figure 23: The sea ice temperatures profiles for four ice cores collected during the cruise *M/V Terra Nordica* Phase II.

5 Sea Ice Salinity:

When sea ice forms, the crystalline material is near pure ice and the saline fraction in the sea water is rejected at the ice/water interface. A fraction of the rejected brine solution is incorporated in the bulk ice material as a network of brine inclusions (Assure & Weeks, 1967). The concentration of brine included in the ice is important in determining the mechanical strength of the resultant ice. At temperatures above the freezing point of the brine (-22 C), these brine networks tend to weaken the ice. All three components of the LIMEX '89 field experiment collected ice cores to make salinity measurements. The cores were sectioned through the ice thickness and the salinity specimens removed and melted. When melted the saline fraction in the ice recombines with the water fraction and yield an homogenous solution which is analyzed for salinity. The *M/V Terra Nordica* phase I cruise salinity readings were conducted with two systems, an optical refractometer and a digital refractometer. On the *M/V Terra Nordica* phase II measurements were conducted with a YSI model 33 salinometer. The salinity profiles illustrate that salinity varies with depth through the ice sheet.

Twenty six cores were sectioned for salinity records. The average salinity was computed for each core and the data sorted into half degree blocks by latitude. Figure 24 presents the sea ice salinities measured for LIMEX 89. The results indicate usual first year ice cover. Ice warming facilities brine migration within the solid ice material. Ice floe which survive a summer season will lose much of it saline content. Typical ice salinities for multi-year ice are less than 1 ppt. and the resultant ice floe are composed of much stronger material.

All the salinity profiles from floes are plotted on Figure 25 to 27. On each graph the profiles are successively offset by 5 ppt. This plotting procedure allows comparison of the shapes of the measured profiles. The profiles are identified at the lower end where the salinity values are well ordered. The identifier gives the J.D. the core was removed and the site number and floe number where the core was taken.

The cores collected during the first phase of the LIMEX '89 experiment were finely sectioned to yield a high resolution for salinity with thickness. Whereas, the cores taken during Phase II, *M/V Terra Nordica* were sectioned into much coarser specimens, to give salinity values to correlate with the sea ice specimens taken for the ice strength measurements. The graphs of the resultant profiles illustrate the different procedures employed to collect the salinity specimens.

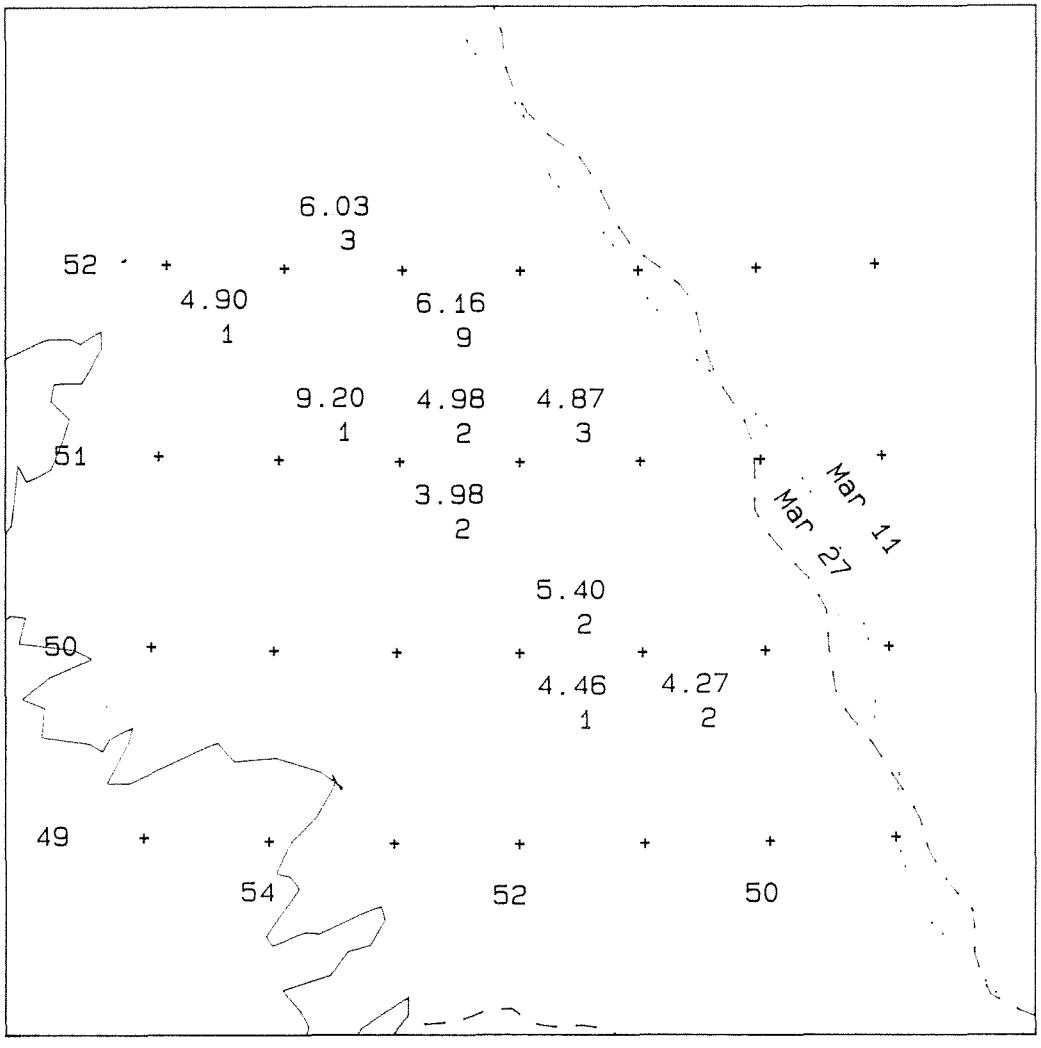

Figure 24: The distribution of mean ice salinities measured, sorted by half degree blocks by latitude. The results are presented as pairs, the upper value the mean thickness and the lower sample count. The map grid covers from *48 N 50 W* to *52 N 56 W*.

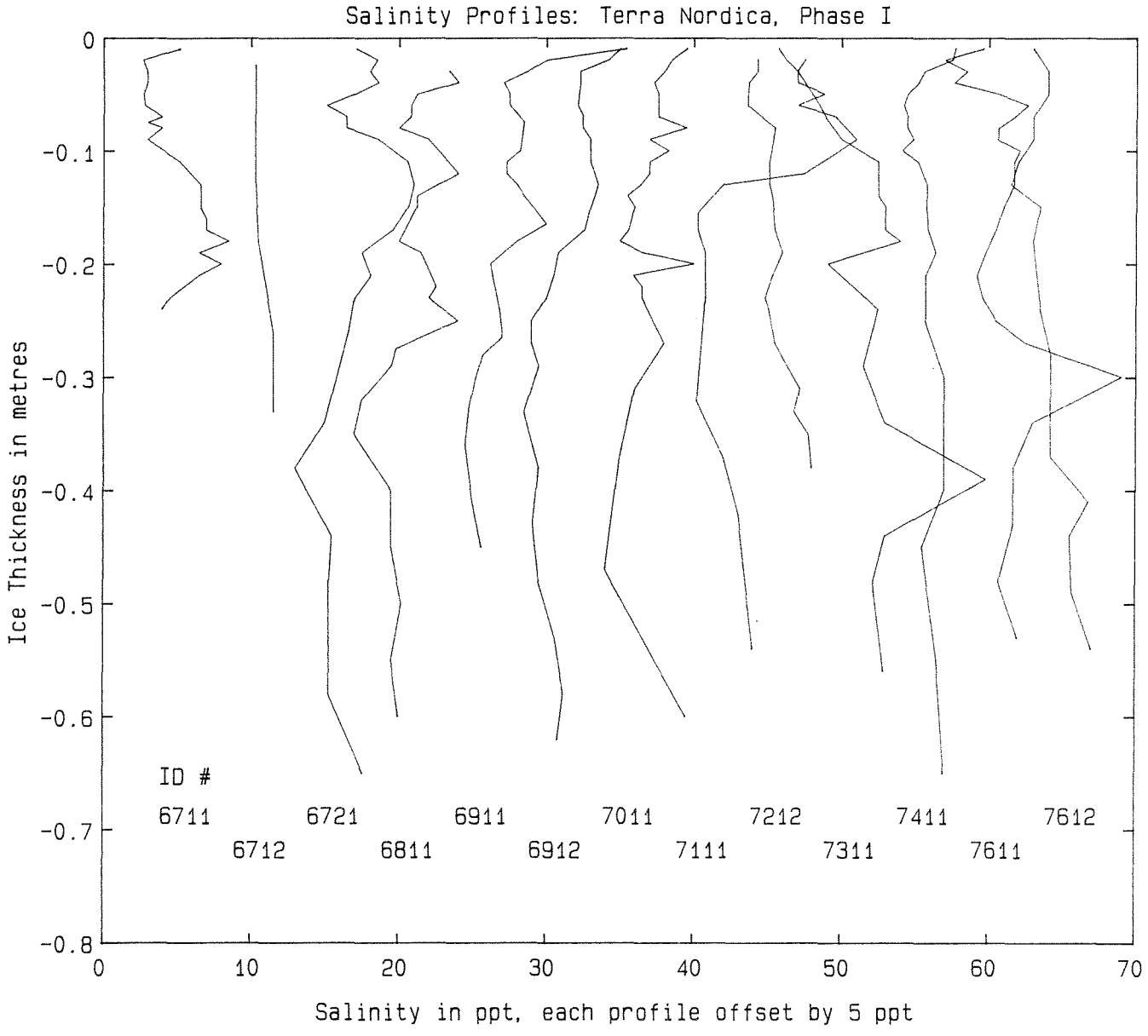

Figure 25: Salinity profiles for sea ice cores collected by researchers during Phase I, *M/V Terra Nordica.*

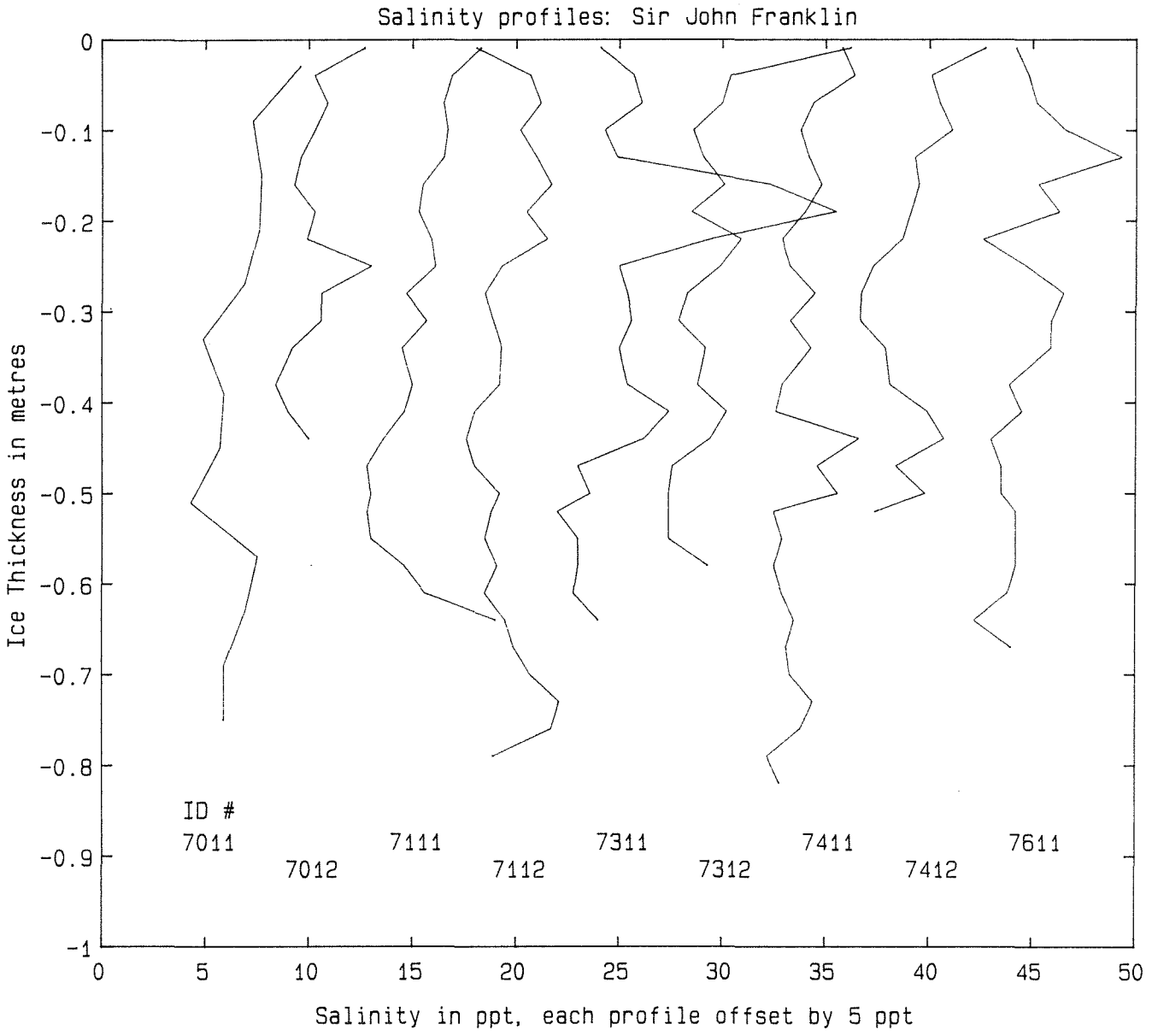

Figure 26: Salinity profiles for sea ice cores collected by researchers on the *CCGS Sir John Franklin*.

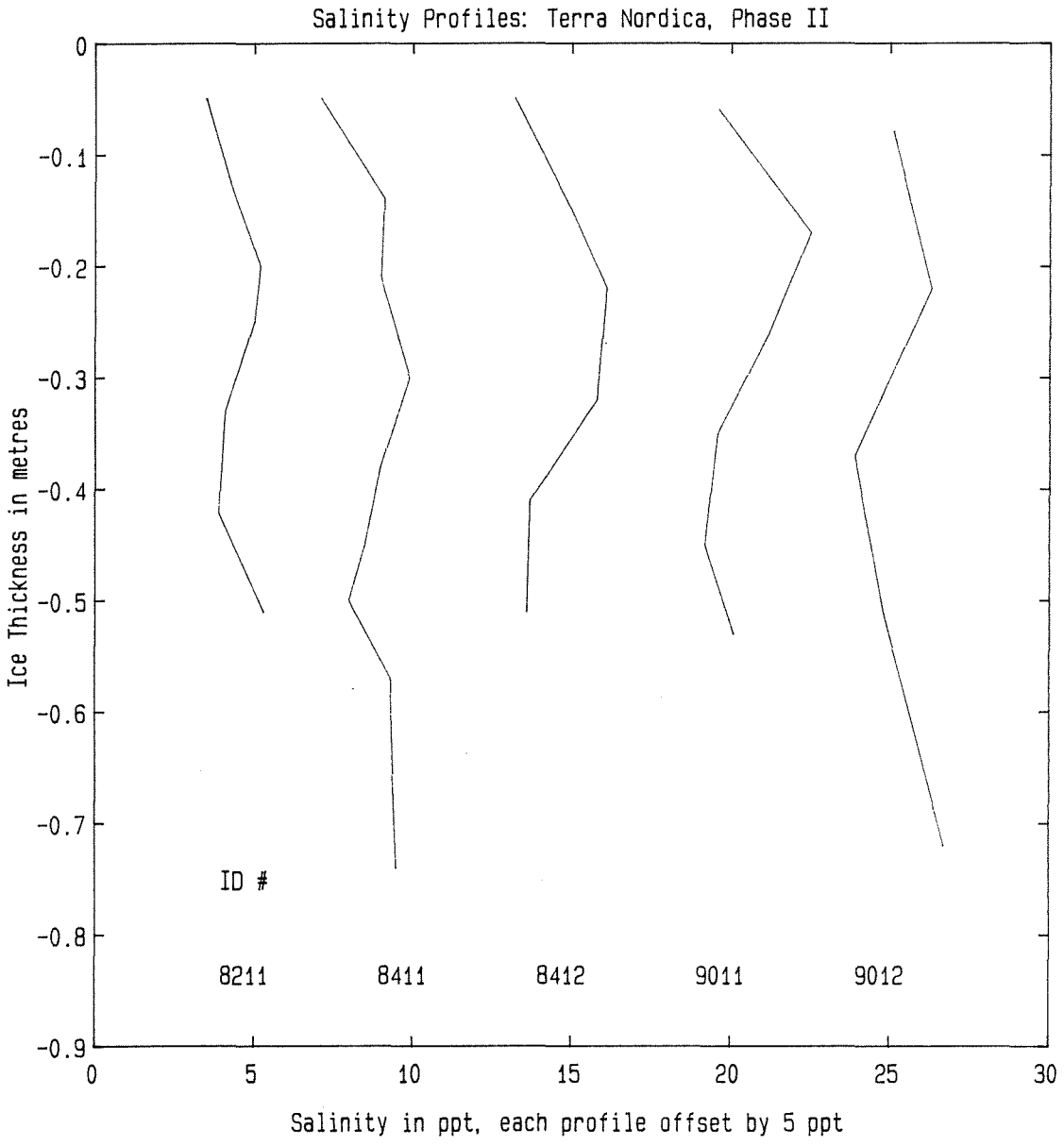

Figure 27: Salinity profiles for sea ice cores collected by researchers during Phase II, *M/V Terra Nordica.*

6 Sea Ice Strength Measurement:

Recent evidence shows that mechanisms such as creep and friction are significant in determining the maximum force that ice can exert when crushed. This project addresses the important phase during crushing in which distributed microcracks are formed, therefore reducing peak stresses. Ice in the Labrador margin is frequently near the melting point through its depth. As a result, creep under applied loads is considerable and enhanced by the formation of grain-sized microcracks during compressive loading.

These experiments represent an initial effort at characterising the crack-enhanced creep properties of sea ice at a temperature of -2 C. Uniaxial compression tests conducted for strain rates of 4×10^{-5} s^{-1} of 3×10^{-4} s^{-1} carried out on ice samples cut from the floes. The samples were unloaded then reloaded at higher and lower rates, therefore characterising the creep properties of the damaged ice. Ice structure, grain size, salinity and density were measured for the test samples.

The earlier section on ice thickness shows the pack ice was 500 mm to 700 mm thick. Crystal structure varied considerably, both spatially within a floe and through the depth. In the top 300 mm, where the ice samples were taken from, most of the ice was of frazil origin, snow ice or refrozen brash ice. There is some evidence of pockets of columnar structure. The viscous properties recorded in these experiments are representative of refrozen brash ice, snow ice and frazil ice near the freezing point that has been damaged during floe collisions. A significant result is that there is not as significant an increase in creep rate with microcracking for the present experiments as for pure granular ice at lower temperatures. Further analysis of damage processes for ice in compression will help to determine the practical implications for determining peak loads. Other implications involve the transmission of energy during floe collisions, although this also requires further experiments at higher loading rates.

6.1 Instrumentation and Test Procedure:

The experiments were conducted in a portable cold room located on the deck of the *M/V Terra Nordica* and finished in the laboratory facilities of the Faculty of Engineering and Applied Science at Memorial University. Compression tests were done on 50 mm, 80 mm, and 200 mm prismatic samples loaded parallel to the longest axis which was also the horizontal plane of the ice surface. All tests were conducted at -2 C, the approximate in-situ temperature of the ice.

Rectangular blocks of ice were cut from the floes using a chain saw. Some brine drainage occurred initially but the blocks were quickly transported to the ship's cold storage area which was maintained between -25 C and -30 C. Similar salinities were recorded later from these blocks which compared favourably to those from the cores sampled from the same floes. The storage period varied from 1 day to 6 weeks at these temperatures. Prismatic samples were cut from these blocks using a 6 mm

bandsaw, measured using callipers and sanded where necessary to meet tolerances. Error in cross-section area was a maximum of 0.5 percent. Tolerance for length was considerably better at 0.1 percent to ensure proper sample alignment. Testing was performed using a Soiltest CT-405 load press with 10,000 lb capacity (Timco and Frederking, 1986). This is an electro-mechanical device capable of constant crosshead speeds resulting in nominal strain rates for the gauge length of 200mm ranging from 4×10^{-5} s^{-1} of 3×10^{-4} s^{-1}. Although a true constant strain rate was not achieved under increasing stress, strain rate was constant for the post-peak plateau stresses used in the subsequent analysis. Strain was measured between the platens using two Schaevitz linear variable displacement transducers (LVDT) mounted at 180 degrees to each other. This form of mounting was chosen because it allowed the recording large strains of distorted samples and allowed reinitialisation of the LVDTs to allow measurement of displacements beyond the ± 5 mm range of the LVDTs. Maximum strains were approximately 0.08. Load was recorded using an Interface 1210 AF 10,000 lb load cell mounted between the upper platen and the load frame. Three data channels were logged at 2.5 Hz to 5 Hz using a Campbell Scientific 21X data logger on the ship and a RTI analog/digital board driven by custom software installed in a Packard Bell microcomputer in the laboratory.

The stiffness of the test machine was determined by repeated loadings and unloadings of a steel sample of known cross-section and was found to be greater than 250 GPa, compared with ice stiffness in the order of 5 GPa. Nevertheless, the important measurements were obtained under approximately constant load in which the machine stiffness is irrelevant and changes in strain rate were negligible.

Linear calibration was applied to both the LVDT and load cell measurements, resulting in maximum measurement errors of 0.03 mm and 130 N respectively. Combined with the geometrical errors, neither the strains nor stresses were more than 3 percent in error from a strict measurement standpoint (at conditions at the platens and temperature variation from test to test because of changing ambient conditions and cycling of the compressor). Perhaps the most significant source of error was due to the natural inhomogeneities in the ice and possible geometrical errors in the sample that allowed eccentric loads and local failure by splitting or concentration of damage along shear planes. Results were ignored where these effects were significant.

Density was measured from 50 mm cubes cut with the bandsaw and sanded to tolerance. Several measurements were made on each face using callipers and the samples were weighed using a mechanical balance. Dimensional tolerances were as noted above, far exceeding errors in the mass, resulting in density errors of approximately 5 kg m^{-3}. Salinity measurements were made from melted samples using a YSI model 33 salinometer to an accuracy of 0.2 ppt. It is expected that a major source of error in the salinity measurements is due to initial brine drainage, although this was reduced by taking samples from the centre of larger blocks.

Thin sections were cut from the density cubes, taking note of the vertical/horizontal orientation. The sections were cut using a bandsaw, stuck to slightly warm plates,

Table 3: Properties of ice specimens for strength testing

sample	density kg m^{-3}	salinity ppt	grn. size mm	depth m	description
16-05-89.04	800	0.52	2	0.20	snow/frazil ice
16-05-89.05	"	"	"	0.20	snow/frazil ice
16-05-89.06	"	"	"	0.20	snow/frazil ice
16-05-89.07	"	"	"	0.20	snow/frazil ice
27-03-89.04	884	3.7	2-3	0.11	frazil ice (cores 4,5)
28-03-89.01	863	4.6	2-3	0.20	"
28-03-89.02	891	3.8	2-3	0.20	"
30-03-89.03	861	"	2-5	0.06	frazil ice

tacked with drops of water, then microtomed to about 0.25 mm to clearly reveal grain boundaries. This same thickness was not possible for the damaged samples, nevertheless particles that were fractions of the original grain size were clearly visible under cross-polarised light. Photographs were recorded on 100 ASA 35 mm colour slide film using a 50 mm macro lens. Grain size was estimated by chord measurements on projected slides.

6.2 Results:

The cores described by Crocker (1989) show that there was a wide variability in the ice structure, spatially within a floe and through the depth of the floes. The analysis of the test samples showed that there was variability in the measured ice densities and that the distribution was bimodal. The density of many samples was approximately 800 kg m^{-3}. These samples contained primarily granular ice (about 2 mm grain size) and were most likely formed as snow ice. On the other hand, the densities of other samples were generally grouped around 880 kg m^{-3}, with a predominantly frazil structure with some columnar ice present. Salinity differences between the two groups were not distinguished. Similarities were found between this ice and that observed by Gow (1987) adjacent to the Labrador coast.

Because of the variety in the tests, only a portion of them are illustrated here and documented in Table 3. The first four samples are from a floe that had ridden up on another floe, therefore resulting in the low salinity value. The remainder are from different locations according to the cores indicated (see Crocker, 1989).

Important features of the ice crushing process were illustrated by the experiments.

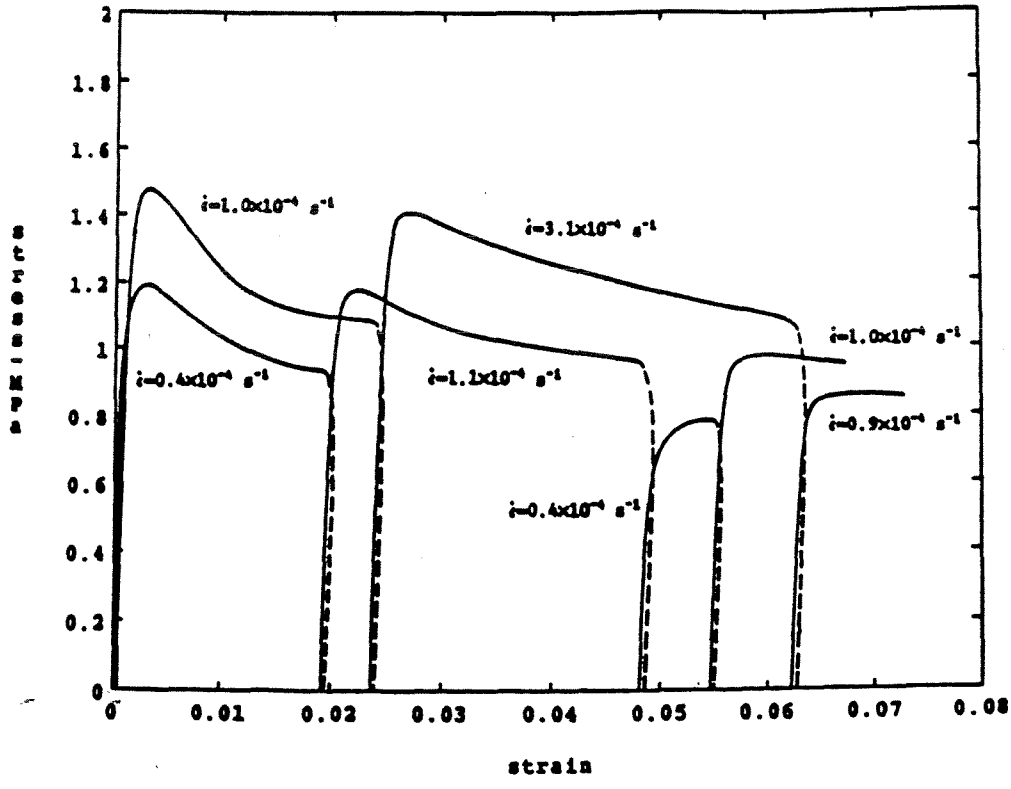

Figure 28: Stress-strain results for uniaxial compression at -2 C: samples 16-05-89.06 and 16-05-89.07.

For a given damaged state, ice can undergo deformation without further damage, as long as the energy input rate is less than what can be dissipated by crack-enhanced creep. Energy input at a higher rate results in further damage as illustrated in Figure 28. Similar behaviour was observed for the two different loading histories.

The axial stress-strain relations were calculated from measured LVDT, load cell and sample geometry data. The stated strain rates were computed from the linear portions of the strain-time relations. It is obvious from the strain-time curves that the strain rate was not constant during the first part of each loading phase, particularly for the initial loading. This is important to bear in mind when trying to model the results. Because displacement was measured from the platens rather than the sample, the recoverable part of the creep could not be measured. This does not however affect the magnitude of the plateau stresses. Furthermore, the plateau stress values do not depend on the recoverable creep strains.

Results from samples 28-03-89.01 and 28-03-89.02 were obtained from reloading at a lower strain rate are given in Figure 29. In all such cases, plateau stresses were

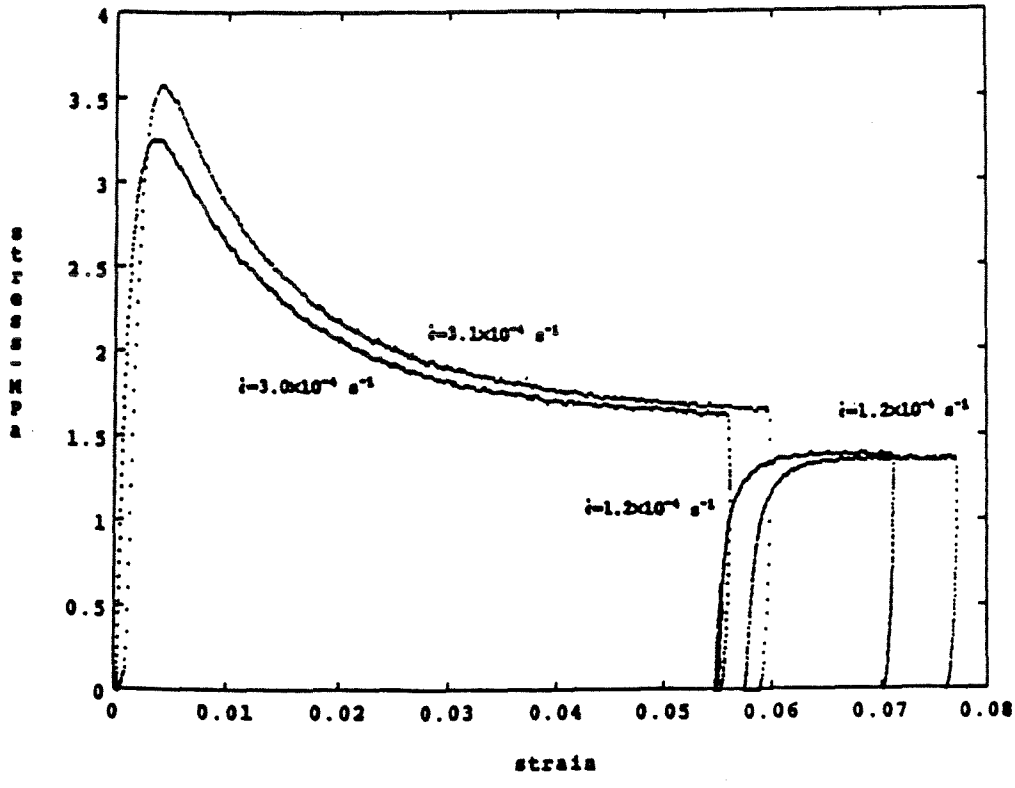

Figure 29: Stress-strain results for uniaxial compression at -2 C: samples 28-03-89.01 and 28-03-89.02.

lower than for the initial loadings. The plateau is indicative of secondary creep which, for both undamaged and damaged ice, is represented by

$$\epsilon_v = f(N)\epsilon_0\sigma^n$$

where ϵ_v is the uniaxial secondary creep rate, ϵ_0 is a temperature dependent creep constant characteristic of the ice, σ is the applies stress (in this case the constant plateau stress) and n is a constant. The function $f(N)$ increases with the crack density N and efforts are currently underway to establish this dependence using laboratory-grown freshwater ice (Sinha, 1988; Stone et al., 1989; Meyssonnier et al., 1989).

The plateau stresses and strain rates for the last four samples identified in Table 3 have been plotted in Figure 30 to illustrate this relation. The creep relation for undamaged freshwater ice corrected to -2 C (Sinha, 1978) is plotted as a solid line. This is an upper bound since brine in the sea ice will enhance secondary creep and evidence indicates that creep at temperatures near the melting point is faster than predicted using a thermal activation correction on lower temperature data. A lower

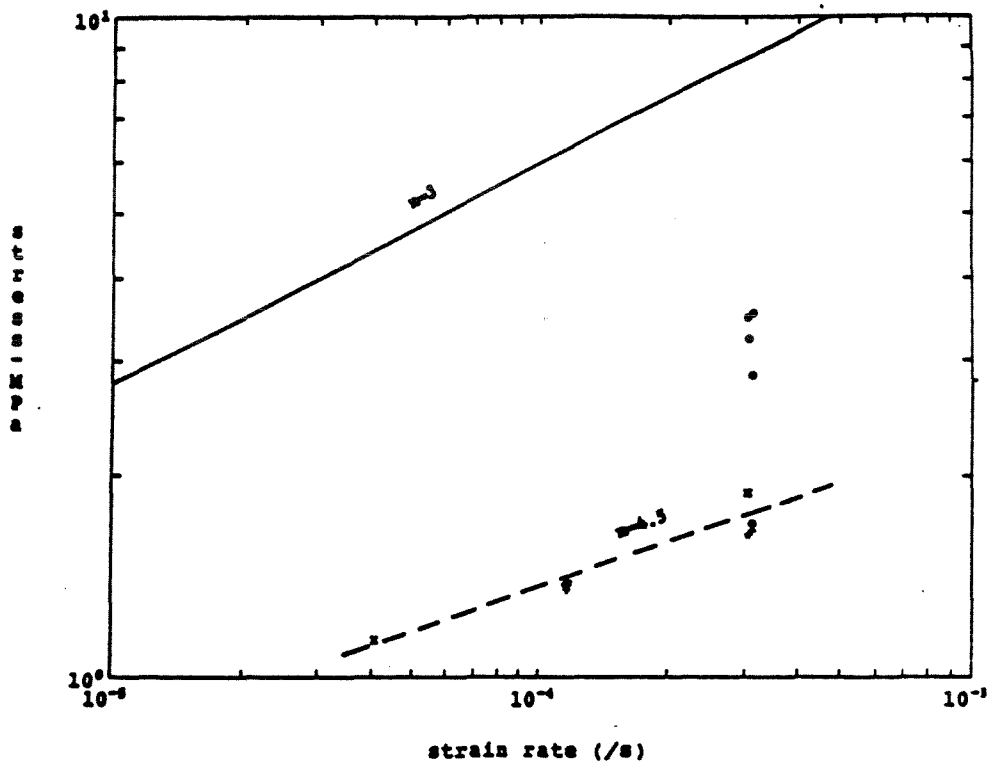

Figure 30: Secondary creep relation for damaged ice from reloading at lower strains: samples 27-03-89.04, 28-03-89.01, 28-03-89.02 and 30-03-89.03 (solid line - freshwater ice at -2 C; solid circles are peak stresses from the initial loading).

bound on the secondary creep for these samples is given by plotting the peak stress from the initial loading (the solid circles in Figure 30). From the present experiments, the exponent n is approximately 4.5, exceeding the value of 3 which is generally accepted for undamaged freshwater ice. The function f(N) for the damaged ice is at as much as 400 based on the freshwater relation and between 15 and 85 based on the maximum peak stress with $n = 4.5$. For initial loading at faster rates, it is possible to exceed these values. Results for the first four samples in Table 3 are given in Figure 31, resulting in $f(N)$ values of 40 relative to the freshwater relation and between 20 and 30 from the maximum of the peak stresses. Note that the creep is more enhanced for the samples which were loaded initially at a higher rate.

Thin sections of the damaged ice revealed that the degree of damage was not uniform throughout the sample. For large strains, there was some localisation of the damage where microcracking produced particles that were 1/2 to 1/5 the original grain size. Also at large strains, some samples formed shear bands of more heavily

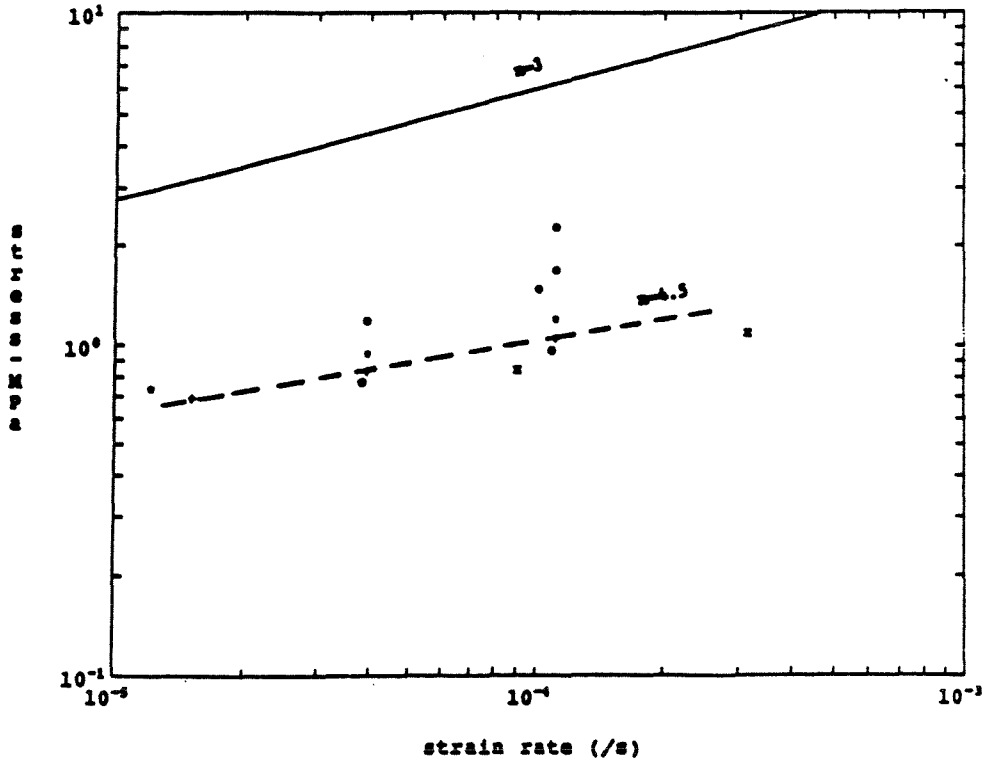

Figure 31: Secondary creep relation for damaged ice from reloading at lower strains: samples 16-05-89.04, 16-05-89.05, 16-05-89.06 and 16-05-89.07 (solid line - freshwater ice at -2 C; solid circles are peak stresses from the initial loading.

damaged material at 45° to 55° from the axis of loading. These are attributed to minor eccentricities in the loading system, and natural defects and inhomogeneities in the samples.

7 Floe Size Characteristics:

A considerable effort has been spent to find a quantitative method to describe the aggregate nature of sea ice cover. In the LIMEX'87 data analysis, floe dimensions were measured for a sample of ice floes on about 100 helicopter aerial photographs. Aside from the fact that the method was extremely labour intensive, that effort illustrated some of the fundamental sampling concerns of trying to describe ice floe size distribution. The decision of the small size cut off between a floe and a piece of brash is critical. This proves to be either an arbitrary decision by the analyst or alternately requires an elaborate set of rules and slows the measurement process. Yet that decision is important because it establishes the number of floes counted and is a factor in the calculation of the mean floes size statistic and the shape of the floe size distribution. The immediate goal is to identify a more robust characteristic. One that is less dependent on subjective decisions by the analyst. The eventual objective would be to automate the measurement process but that will require considerable effort due to the nature of sea ice cover imagery.

Digital image processing is being used to evaluate methods to estimate ice floe size distribution. Most remote sensing image analysis is based on tonal information of the imagery. The ice features we are attempting to identify: floe entities, floes shapes, floe population density, are distinguished by the human observer's ability to interpret the context of the scene. Experiments utilizing tonal classification were used to estimate ice/water fraction and floe ice fraction. Density slicing fails to classify a scene into distinct floe entities. Touching floes general join for binary classified scenes even though the individual floes appear as distinct entities in multi-level tonal scenes. This dilemma will be explored by further research.

Edge density is proposed as a method to estimate floe size distribution. A sea ice cover composed of floes displays a certain density of linear floes edges per unit area of ice cover. The edge density is proportional to the sizes and the shapes of the sea ice floes which form the ice cover.

This is a straightforward method to implement on an image processing system. Again the measurement relies on an analyst. The observer makes classification decisions based on the context of the displayed ice scene. The ice cover imagery was collected by a vertically looking S-VHS video camcorder. The camera was mounted inside the cab of the helicopter and aim through the clear panel in front of the passenger seat. The helicopter proves to be a poor camera platform because of the low accuracy of camera height measurement.

A Hewlett Packard Vectra RS/20C microcomputer equipped with a MATROX PIP-640 frame-grabber board installed, was employed to digitize the images collected on video tape. A video frame collected in 1/30 second, is composed of two interlaced video fields. The video camera CCD is shuttered on the field rather than the frame. Therefore the digitized video frame is made up of two interleaved scenes photographed from two points separated by the distance the helicopter travelled in

1/60 of a second. This information provides an independent check of the helicopter height for low altitude scenes.

Therefore the images need to be processed to separated the two image fields. Single fields are used to supply the image data extracted for this report. Simple translation of the two fields did not merge the two images. It would be straightforward to correct the superimposed images for aircraft roll (translation of the horizontal lines) but it will be less practical to compensate for yaw when the platform yaw is significant between two fields. Decomposing by field results in a 50 percent loss of vertical resolution. But it makes significant improvement in the visual appearance of the scene.

The histogram of pixel values are employed to establish the contrast of the original scene. When the actual dynamic range of a scene is low compared with the 256 levels available, a contrast stretch is implemented to enhance the visual appearance of the image. Then a classification algorithm is implemented to first separate the scene into ice/water fractions. The analyst's judgement is applied to decide when the ice/water fraction matches the image scene. This is followed a classification of ice floe fraction for the scene. The classification algorithm is employed but the threshold is adjusted until the scene is divided by the ice floe boundaries. A three by three median filter is employed to complete the classification into ice/water fraction for the first case and ice floe fraction in the second case. Then a Prewitt three by three edge filter is implemented to emphasis the ice floe boundaries. Each scene is saved to a disk file and then used as input to compute the ice/water, ice floe and ice edge fraction for each scene.

The present version of the edge filter produces an edge pattern that is more than a single pixel width. Two sub-scenes were digitized to provide a conversion factor to transform the edge scene value from edge pixel fraction to linear edge density. The result of this analysis is provided for 11 scenes, see Tables 4 and 5. The outcome of the analysis suggest that the small floe (brash) threshold continues to be a critical factor. This inherent problem relate to quantization of the digital image. A one metre diameter is represented by one or two pixels in a ice cover scene collected at 305 metres altitude and 100 to 150 pixels in area from an overflight at 40 metres. Therefore low altitude vertical video provide very limited coverage. Only one good aerial flight line was collected during LIMEX'89. Video lines can be mosaicked into extended line scans but would be a labour intensive task employing the existing image analysis system. A line scan would provide a valid estimate for the ice/water fraction and the ice floe fraction in the ice cover. These initial results indicate that ice edge density yields a single value to characterize floe size distribution. A theoretical study is needed to establish a formal relationship between edge density and floe size distribution.

Table 5 indicates the edge density relatively invariant for scenes of similar altitude. This does not negate the premise of the section because the floe size distribution appears similar along the JD 90 (March 31), 1989 flight line. It is difficult to compare

Table 4: The ice floe, brash and water fractions from pack ice scenes.

#	time	lat	long	ice conc. %	open water %	ice floes %	brash ice %
11	82.65	49.99 N	52.43 W	99.09	0.91	73.86	25.23
12	82.65	49.99 N	52.43 W	98.27	1.73	79.86	18.41
08	84.48	49.55 N	51.87 W	95.81	4.19	72.44	23.37
06	90.37	50.03 N	52.37 W	96.92	3.08	66.30	30.62
07	90.67	50.02 N	52.03 W	96.95	3.05	63.00	33.95
09	90.68	50.00 N	51.66 W	96.79	3.21	73.20	23.59
10	90.73	50.00 N	51.37 W	91.30	8.70	60.11	31.18
14	92.24	49.78 N	50.78 W	97.93	2.07	79.02	18.91
03	92.85	49.83 N	50.87 W	79.87	20.13	54.94	24.93
04	92.85	49.83 N	50.87 W	94.94	5.06	72.18	22.76
13	92.88	49.77 N	50.89 W	95.78	4.22	76.07	19.71

Table 5: Floe Sizes and Edge Densities

#	time	lat	long	scene area m^2	no. floes	floe area m^2	edge density m/m^2
11	82.65	49.99 N	52.43 W	9,800	118	61	0.525
12	82.65	49.99 N	52.43 W	9,800	124	63	0.421
08	84.48	49.55 N	51.87 W	4,650	75	45	0.747
06	90.37	50.03 N	52.37 W	38,100	237	106	0.346
07	90.67	50.02 N	52.03 W	38,100	203	118	0.323
09	90.68	50.00 N	51.66 W	38,100	373	74	0.275
10	90.73	50.00 N	51.37 W	38,100	217	105	0.350
14	92.24	49.78 N	50.78 W	9,200	145	50	0.458
03	92.85	49.83 N	50.87 W	9,180	102	50	0.881
04	92.85	49.83 N	50.87 W	9,180	93	71	0.552
13	92.88	49.77 N	50.89 W	9,950	137	55	0.489

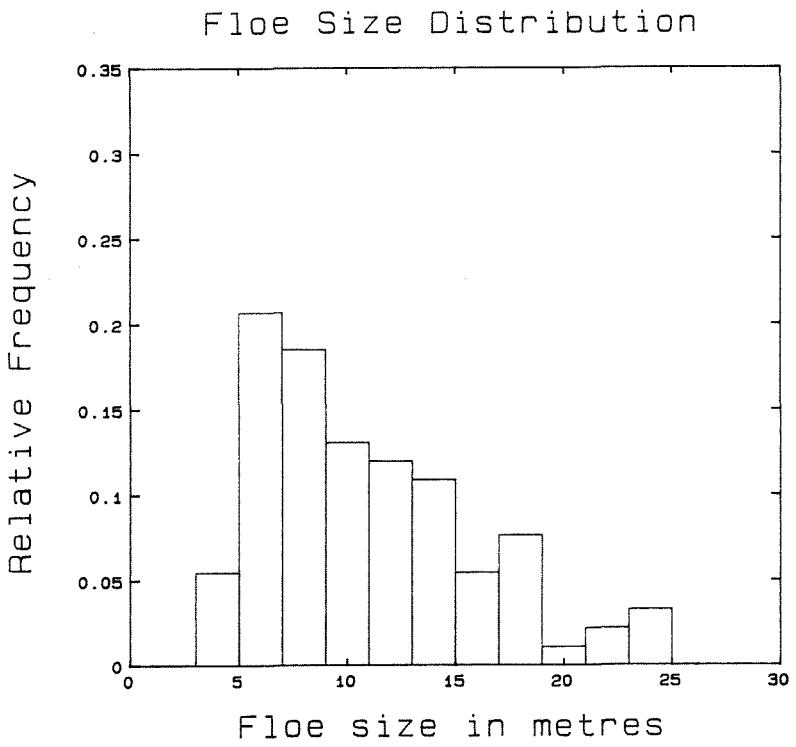

Figure 32: Floe size distribution for a scene of aerial video collected March 31, 1989, altitude 305 m, scene LXICE06.IMG.

the values collected during the other overflights because they were collected from different altitudes.

Four scenes from the helicopter video line collected on March 31, 1989 (J.D. 90) were adapted to estimate floe size distribution for the ice cover encountered. 341 $\times$ 441 pixel digital images (130 $\times$ 154 m) were extracted, enhanced to give good contrast and printed. Line segments representing the major and minor axes were digitized for every floe greater than 10 pixel units in each scene. The average floe dimensions were calculated from the digitized points. These example floesize distributions are plotted in Figures 32 to 35. The distribution for scene LXICE09, Figure 34 indicates a more broken sea ice cover with a smaller mean floe size and a smaller floe dimension variance.

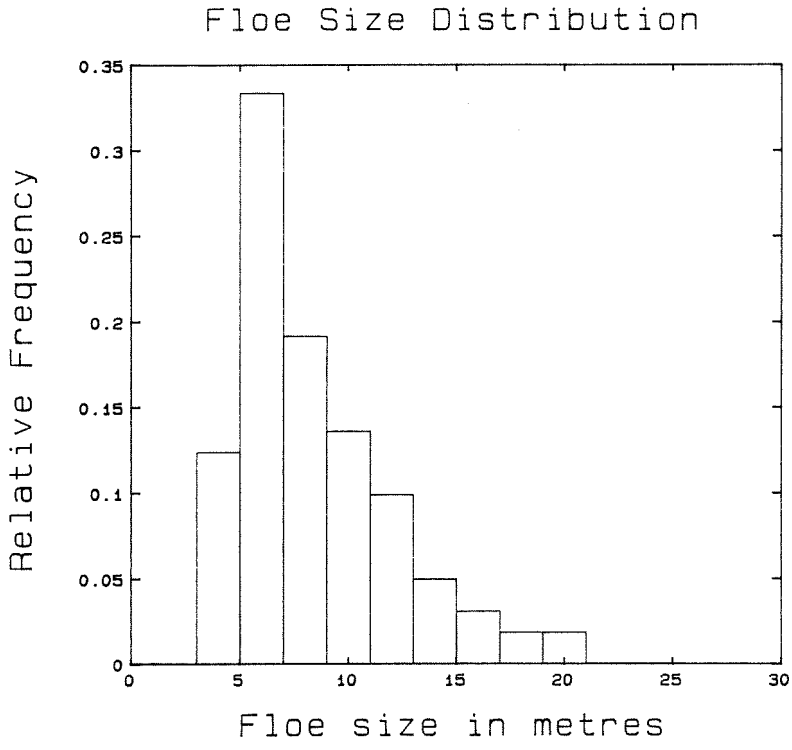

Figure 33: Floe size distribution for a scene of aerial video collected March 31, 1989, altitude 305 m, scene LXICE07.IMG.

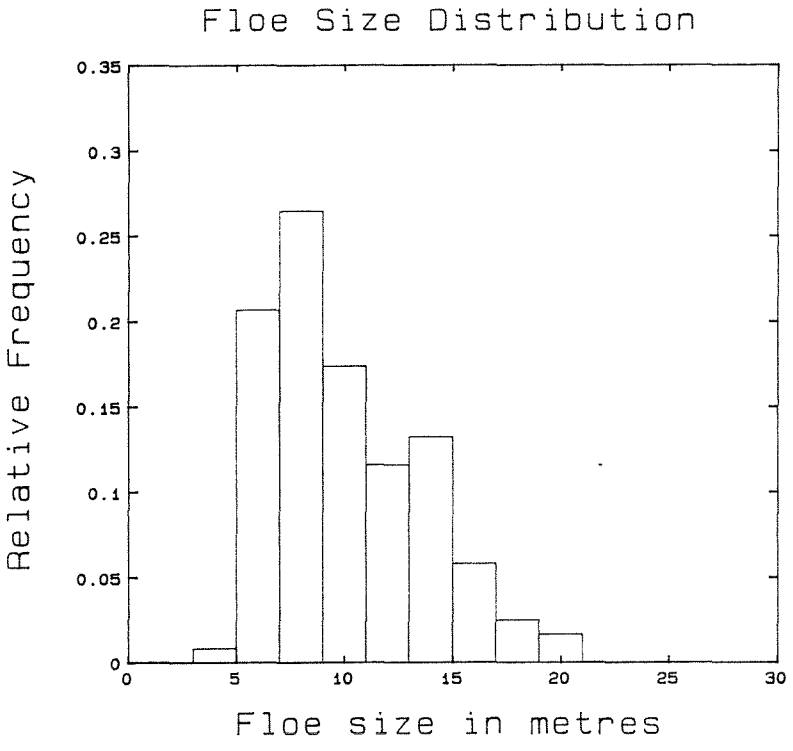

Figure 34: Floe size distribution for a scene of aerial video collected March 31, 1989, altitude 305 m, scene LXICE09.IMG.

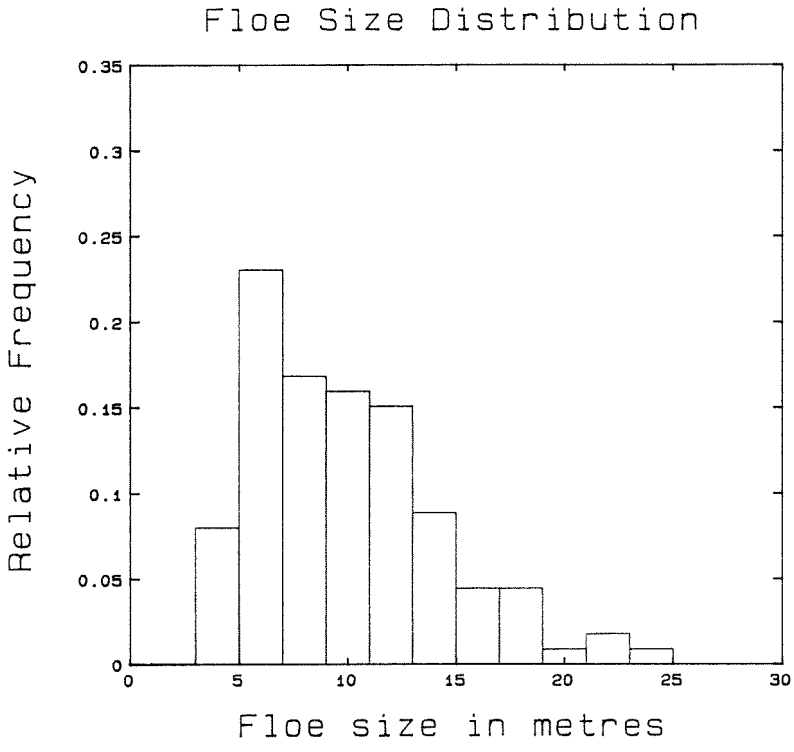

Figure 35: Floe size distribution for a scene of aerial video collected March 31, 1989, altitude 305 m, scene LXICE10.IMG.

References

[1] Carsey, F.D., Argus, S.A., Collins, M.J., Holt, B., Livingston, C.E., and Tang, C.L. (1989) "Overview of LIMEX '87 Ice Observations", IEEE Transactions on Geoscience and Remote Sensing, Vol. 27, pp468-482.

[2] Crocker, G.B. (1989) "Ice Characteristics", Section 8.9 of the **LIMEX 89 Data Report.**

[3] Gow, A.J. (1987) "Crystal Structure and Salinity of Sea Ice in Hebron Fiord and Vicinity, Labrador", CRREL Report 87-4, 18p.

[4] Jensen, John R., (1986) **Introductory Digital Image Processing, A Remote Sensing Perspective**, Prentice-Hall, Englewood Cliffs, New Jersey.

[5] Meyssonnier, J. and Duval, P. (1989) "Creep Behaviour of Damaged Ice under Uniaxial Compression: a Preliminary Study", Proceedings of the 10th International Conference on Port and Ocean Engineering under Arctic Conditions, Lule, Sweden, 12-16 June 1989, in press.

[6] Nazarenko, Dennis and Lapp, David (1989) "Ice Characterization Studies from the *CCGS Sir John Franklin*", Section 7.7 of the **LIMEX 89 Data Report.**

[7] Sinha, N.K. (1978) "Rheology of Columnar-grained Ice", Experimental Mechanics, Vol.18, No.12, pp.464-470.

[8] Sinha, N.K. (1988) "Crack-enhanced Creep in Polycrystalline Material: Strain-rate Sensitive Strength and Deformation of Ice", Journal of Materials Science, Vol.23, No.12, pp.4415-4428.

[9] Stone, B.M., Jordaan, I.J., Jones, S.J. and McKenna, R.F. (1989) "Damage of Isotropic Polycrystalline Ice under Moderate Confining Pressures", Proceedings of the 10th International Conference on Port and Ocean Engineering under Arctic Conditions, Lule, Sweden, 12-16 June 1989, in press.

[10] Timco, G.W. and Frederking, R.M.W. (1986) "Confined Compression Tests: Outlining the Failure Envelope of Columnar Sea Ice", Cold Regions Science and Technology, Vol.12, pp.13-28.